

This is a non-peer reviewed pre-print submitted to EarthArXiv. This manuscript is currently under review at the journal *Nature*.

Subsequent versions of this manuscript may have slightly different content.

We welcome feedback. Please contact Matt Osman
(mattosman@arizona.edu) regarding this manuscript's content.

Globally resolved surface temperatures since the Last Glacial Maximum

Matthew B. Osman^{1*}, Jessica E. Tierney¹, Jiang Zhu², Robert Tardif³, Gregory J. Hakim³, Jonathan King¹, Christopher J. Poulsen⁴

¹*Department of Geosciences, The University of Arizona, Tucson, AZ 85721, USA*

²*Climate and Global Dynamics Laboratory, National Center for Atmospheric Research, Boulder, CO 80305, USA*

³*Department of Atmospheric Sciences, University of Washington, Seattle, WA 98195, USA*

⁴*Department of Earth and Environmental Sciences, University of Michigan, Ann Arbor, MI 48109, USA*

*To whom correspondence should be addressed: mattosman@arizona.edu.

Climate changes across the last 24,000 years provide key insights into Earth system responses to external forcing. Climate model simulations ^{1,2} and proxy data ³⁻⁸ have independently allowed for study of this crucial interval; however, they have at times yielded disparate conclusions. Here, we leverage both types of information using paleoclimate data assimilation ^{9,10} to produce the first observationally constrained, full-field reanalysis of surface temperature change spanning the Last Glacial Maximum to present. We demonstrate that temperature variability across the last 24 kyr was linked to two modes: radiative forcing from ice sheets and greenhouse gases; and a superposition of changes in thermohaline circulation and seasonal insolation. In contrast with previous proxy-based reconstructions ^{6,7} our reanalysis results show that global mean temperatures warmed between the early and middle Holocene and were stable thereafter. When compared with recent temperature changes ¹¹, our reanalysis indicates that both the rate and magnitude of modern observed warming are unprecedented relative to the changes of the last 24 kyr.

1 The interval of time spanning the Last Glacial Maximum (LGM; 21–18 ka) to the preindustrial
2 era represents the most recent large-scale reorganization of the climate system, during which the
3 Earth rapidly transitioned out of a cold, glaciated state with vast Northern Hemisphere ice sheets
4 into a warm interglacial. Constraining the evolution of global surface temperatures during this
5 critical time period provides an excellent opportunity to better understand the mechanisms of large-
6 scale climate change, including Earth system interactions and responses to various forcings (e.g.,
7 greenhouse gases, albedo/ice-sheet, and orbital changes).

8 A number of prior studies have attempted to characterize the global surface temperature evo-
9 lution from the LGM to present ^{3–7}. Of particular note, Shakun et al. ³ and Marcott et al. ⁶ estab-
10 lished a global mean surface temperature (GMST) estimate spanning the deglacial and Holocene
11 periods using a limited ($n \leq 80$), globally dispersed marine and terrestrial temperature proxy
12 database (hereafter, the Shakun-Marcott Curve; SMC). However, subsequent comparisons of SMC
13 to both independent temperature reconstructions and transient LGM-to-present model simulations,
14 such as TraCE-21k ^{1,12}, revealed discrepancies surrounding the abruptness, magnitude, and rapid-
15 ity of deglacial global warming ^{2,4,12}, as well as the phasing and magnitude of millennial-scale
16 deglacial cooling events ^{1,13,14}. One of the most prominent differences between SMC and climate
17 model simulations is the direction of global temperature change across the Holocene. Whereas
18 SMC shows a cooling trend, modeling results indicate there should be a warming, a phenomenon
19 termed the “Holocene Temperature Conundrum” ². More recent work has sought to reconcile
20 these differences by using either independent ^{5,15} or additional ^{7,15} proxies, and by correcting for
21 possible proxy seasonal biases ^{2,8,15}. Nonetheless, all of these approaches have a fundamental lim-
22 itation in that none provide a dynamically consistent full-field view of climate evolution since the
23 LGM. Conversely, although climate models provide a self-consistent and spatially complete repre-
24 sentation of the climate system, they are known to have biases due to inaccurate representation of
25 climate processes. Additionally, the fidelity of paleoclimate simulations of the LGM and Holocene
26 depends on the accurate knowledge of paleoclimate boundary conditions, which are known with

27 varying levels of certainty ^{2,16,17}.

28 **The Last Glacial Maximum Reanalysis**

29 Here, we revisit the evolution of global temperatures from the LGM to present using an offline pa-
30 leoclimate data assimilation approach that formally combines proxy and model information ^{9,10,18}.
31 The resulting “Last Glacial Maximum Reanalysis” (LGMR) product offers a complete spatiotem-
32 poral view of climate change for the last 24 kyr. The LGMR enables us to diagnose the major
33 modes of climate variability, refine our understanding of global temperature changes across the
34 Holocene, and compare the current anthropogenic global warming with the rate and magnitude of
35 change seen in the recent geological record.

36 Following ref. ¹⁰, we focus on assimilating geochemical proxies for sea-surface temperature
37 (SST) with established Bayesian forward models ^{19–22}. To ensure that the proxy data had sufficient
38 temporal resolution and length to inform our reconstruction, we required that records be at least
39 4,000 years long, have a median time resolution of 1,000 years or less, and contain a radiocarbon-
40 based age model. The temporal criteria were relaxed for sites in the Southern Ocean to increase
41 coverage in this data-poor region. Conversely, some SST records that met these criteria were ex-
42 cluded due to complications related to proxy interpretation and (or) their location (see Methods). In
43 total, our vetted compilation consists of 539 records, including 133 alkenone ($U_{37}^{K'}$), 25 TetraEther
44 indeX of 86 carbons (TEX₈₆), 123 planktic foraminiferal Mg/Ca, and 258 planktic foraminiferal
45 oxygen isotope ($\delta^{18}O_c$) time series (Fig. 1 and Extended Data Figure 1).

46 Our proxy compilation provides unprecedented insight into LGM-to-present climate evolu-
47 tion on its own, but transient offline data assimilation further leverages the full-field dynamical
48 insights available from climate model simulations and bypasses issues related to heterogeneous
49 proxy spatial distribution ^{3,4,6–8}. The model simulations used for the assimilation consist of 17
50 LGM-to-present time-slice experiments conducted with the isotope-enabled Community Earth
51 System Model version 1 (iCESM1; Extended Data Table 1 and Methods; ^{10,23}). We draw an

52 ensemble of 50-yr average states from these simulations for our model "prior". The model prior
53 includes all of the variables needed by our proxy forward models (monthly salinity and SST, and
54 mean-annual $\delta^{18}\text{O}$ of seawater; Methods) as well as other variables of climatic interest including
55 mean annual surface air temperature (SAT) and the $\delta^{18}\text{O}$ of precipitation ($\delta^{18}\text{O}_p$). We reconstruct
56 climate at 200-year intervals, adhering to the resolution limitations of the majority (>90%) of our
57 proxy data. For a given time interval, we estimate proxy values from the model prior at the lo-
58 cations where geochemical measurements exist using Bayesian forward models (Methods). The
59 difference between the actual proxy value and the forward modeled value (the "innovation") is
60 first weighted by the Kalman gain—which considers the covariance between the proxy location
61 and the climate fields as well as uncertainties in the proxies and the prior—and is then added to the
62 model prior state. For our final reconstruction, we produced a posterior ensemble of 300 realiza-
63 tions, based on sampling 60 representative prior iCESM states for each time interval (Methods),
64 with 20% of proxy records randomly withheld for error quantification and validation testing. For
65 each ensemble member, we also sampled age uncertainty to ensure that this source of error was
66 propagated into our assimilated fields (Methods).

67 The LGMR highlights the exceptional and spatially heterogeneous nature of deglacial cli-
68 mate change (Fig. 2). Reconstructed global mean surface temperature (GMST) reveals a signifi-
69 cant ($p < 0.05$; Methods) three-part sequence across the last 24 ka. From 24–17 kyr BP, the Earth
70 is in a ubiquitously cold glacial state. The thermal imprints of the North American and Eurasian
71 ice sheets are near their maximum extent, with terrestrial cooling relative to the pre-industrial in
72 excess of -20°C across the glaciated high northern ($>45^\circ\text{N}$) and southern ($>45^\circ\text{S}$) latitudes (Fig.
73 2). At 17.2 ka (95% CI = 18.7–16.4 ka, Methods), global-scale deglaciation (the second stage)
74 abruptly begins. Deglacial global warming shows a familiar ³ two-step rise that is punctuated
75 by the millennial-scale Bølling-Allerød (14.8–12.8 ka) to Younger Dryas (12.8–11.7 ka) events.
76 Following the Younger Dryas cold spell, the Earth enters its final transition towards the present
77 interglacial. In the third part of the GMST sequence, gradual early Holocene (11 kyr BP onward)

78 warming stabilizes to near pre-industrial temperatures (i.e., within $\sim 0.5^\circ\text{C}$) by 9.2 ka (95% CI =
79 11.0–8.3 ka). A vestigial cold imprint atop northeastern North America is all that remains of the
80 once-great Northern Hemisphere ice sheets as mild, albeit widespread, high-latitude warming en-
81 sues; Antarctica now shows a notable east-west thermal dipole next to a relatively warm Southern
82 Ocean, whereas mild cooling persists across much of the tropics (Fig. 2). All told, we estimate a
83 mean global warming of $6.8 \pm 0.8^\circ\text{C}$ (2σ) from the deglaciation onset at 17.2 ka to pre-industrial,
84 broadly in line with, though slightly larger than, the value reported in ref. ¹⁰ (6.1°C). The greater
85 warming found here reflects the LGM period referenced (ref. ¹⁰ uses 23–19 kyr, which includes
86 mildly warmer GMST according to the LGMR) as well as differences in iCESM model priors and
87 proxy data distribution (Methods).

88 **Validating the LGMR**

89 We objectively test the skill of the LGMR using two independent methods of statistical valida-
90 tion. First, we use our posterior LGMR fields to reconstruct the randomly withheld proxy time
91 series (e.g., ref. ¹⁸). Across the ensemble, we find that the majority of records are skillfully re-
92 constructed with no obvious signs of regional bias, suggesting that our posterior assimilation is
93 robust (Extended Data Figure 2; Methods). Second, following ref. ¹⁰, we compare posterior $\delta^{18}\text{O}_p$
94 to independent ice core- and speleothem-derived $\delta^{18}\text{O}$ time series (Extended Data Table 2). On a
95 global scale, we find notable improvement in the posterior comparison of $\Delta\delta^{18}\text{O}_p$ over the prior
96 state, with a $\sim 30\%$ reduction of bias and a large increase in variance explained (Extended Data
97 Figure 3). In particular, the millennial-scale correspondence of the ice core records with LGMR
98 $\delta^{18}\text{O}_p$ is remarkable, with R^2 values ranging from 0.65 to 0.90 ($n = 14$ records; Extended Data
99 Table 2, Extended Data Figure 4).

100 Drivers of global SAT change

101 To gain further insight into the drivers of global surface temperature change during the last 24
102 ka, we decompose our LGMR temperature fields into spatiotemporal modes of variability using
103 Empirical Orthogonal Function (EOF) analysis, following past studies that relied solely on proxies
104 ^{24,25}. As expected, the first spatial mode, EOF1, exhibits positive loading across the globe and
105 explains the overwhelming majority (>90%) of the surface temperature covariance during the last
106 24 ka (Fig. 3a). This mode is clearly associated with deglaciation, with the strongest amplitude
107 concentrated atop the North American and Fennoscandian ice sheets. The unimodal nature of
108 EOF1 implies an association with changes in greenhouse gas (GHG) radiative forcing and ice sheet
109 albedo. Given the monotonic nature of the associated principal component time series, PC1, GHG
110 forcing ²⁶ can explain 93% of the EOF1 variance (Fig. 3b). However, there are notable differences
111 in the two time series; during the early- to mid-Holocene, GHG radiative forcing increases at ca.
112 12 ka and then gradually decreases, while PC1 steadily increases, indicating a steady increase in
113 global temperature. This implies GHG forcing alone is not sufficient for explaining the leading
114 mode of global temperature variability.

115 Modeling experiments indicate that the magnitude of ice sheet albedo forcing is comparable
116 to (if not greater than) GHG forcing across the deglacial transition ^{10,27,28}. By considering GHG
117 and ice sheet forcing together, we account for >99% of the variance in PC1 as well as the observed
118 warming from the early to mid-Holocene (Fig. 3c). The inclusion of ice sheet albedo forcing also
119 explains the strong EOF1 loading atop North America and Fennoscandia (Fig. 3a). While we
120 acknowledge that other radiative forcings, such as vegetation and dust, likely impacted LGM-to-
121 present temperature change ¹⁰ our EOF results imply that these were probably of second-order
122 importance in terms of their climatic footprint, particularly during deglaciation.

123 The second mode of global temperature variability, EOF2, explains only ~3% of the vari-
124 ance. However, it is distinct from its neighboring tailing modes ²⁹ and physically interpretable.

125 This mode is a hemispheric dipole, with strong positive loading across the Southern Hemisphere
126 (especially in the Southern Ocean) and negative loading spanning much of the Northern Pacific,
127 North America, and the North Atlantic. Its associated time series, PC2, consists of both long-term
128 trends as well as millennial-scale peaks during the deglaciation. We interpret this mode to repre-
129 sent a superposition of two sources of climate variability: thermohaline circulation changes (the
130 millennial-scale features) and shifts in high-latitude seasonal insolation (the long-term trends). To
131 illustrate this, we decompose PC2 into its “trend” (Fig. 3c, purple) and “residual” (Fig. 3c, yellow).

132 The trend-component of PC2 represents a precession cycle, with a peak at ca. 11 ka. Both
133 summer insolation intensity at 65°N³⁰ and Southern Hemisphere summer duration at 65°S³¹ offer
134 good approximations of this long-term change (Fig. 3c). The spatial pattern of EOF2, however,
135 which shows positive loading in the Southern Ocean and negative loading in the Northern Hemi-
136 sphere (Fig. 3b), suggests that Southern Hemisphere summer duration is the likely driver. It is
137 unclear how enhanced summer insolation in the Northern Hemisphere would lead to mean annual
138 cooling, given that this conflicts with conventional Milankovitch orbital theory³²). In addition,
139 spatial correlation analyses (of either orbital series) with surface temperatures indicate that the
140 tightest coupling occurs in the Southern Hemisphere (Extended Data Figure 5b). The strong load-
141 ing of EOF2 in the Southern Ocean in particular could point towards a feedback with regional sea
142 ice; a longer summer (and shorter winter) would increase the extent of summertime sea ice retreat
143 while decreasing its growth during wintertime, resulting in an increase in mean annual surface
144 temperatures³¹.

145 The residual-component of PC2 closely follows ($R^2 = 0.80$) ²³¹Pa/²³⁰Th proxy records of
146 Atlantic Meridional Overturning circulation (AMOC) from the Bermuda Rise^{33–35} (Fig. 3c). Prior
147 studies have also identified this “bipolar seesaw” mode^{24,25}, which represents the millennial-
148 scale events that occur during the last deglaciation (Heinrich event 1, the Bølling-Allerød, and
149 the Younger Dryas). Correlation analysis shows that Northern Hemisphere surface temperatures in

150 LGMR are strongly related to AMOC changes (Extended Data Figure 5c). A decrease in Atlantic
151 heat transport would also lead to compensating warmth in the Southern Hemisphere, similar to
152 what we observe in the loading pattern of EOF2. However, the particularly strong loading we ob-
153 serve across the Indian and Pacific ocean sectors of the Southern Ocean does not match the classic
154 fingerprint of the oceanic bipolar seesaw³⁶. Similarly, the strong loading in the eastern North Pa-
155 cific is not typical of a modeled response to an AMOC slowdown^{1,12,37}. It does, however, reflect
156 the underlying proxy records from this region, which show a strong response of SST to North At-
157 lantic climate variability³⁸. It also conforms to recent suggestions that Columbia River megaflood
158 meltwater forcing might have contributed to the severe cooling observed in deglacial SST records
159 from the Gulf of Alaska¹³.

160 **Comparison to proxy-only insights**

161 LGMR GMST shows several notable differences when compared to the proxy-only SMC recon-
162 struction (Fig. 4a). Focusing first on pre-Holocene differences, the LGMR has 1) a more abrupt
163 onset of deglaciation at ~ 17.2 ka; 2) a more muted Bølling-Allerød–Younger Dryas transition; and
164 3) nearly twice as much glacial cooling (Fig. 4). The latter difference can be explained by the fact
165 that the SMC is mostly based on SST proxies and was not scaled to infer GMST (i.e., ref. ⁴). To
166 diagnose the origin of the other differences, we generated a proxy-only GMST reconstruction from
167 our SST compilation (Methods). Even though our compilation has many more proxy SST records
168 than SMC (and no terrestrial records), it is remarkably similar ($R^2 = 0.97$; Fig. 4a).

169 The similarity of the proxy-only reconstruction and the SMC illuminates at least two short-
170 comings that are effectively mitigated by our data assimilation approach. Proxy-specific GMST
171 reconstructions (Extended Data Figure 6) suggest that the gradual deglacial onset is most likely
172 linked to the Mg/Ca data, which show early deglacial SST increases and a sustained warm bias
173 relative to $\delta^{18}\text{O}_c$ and (to a lesser extent) $U_{37}^{K'}$ (Extended Data Figure 6). Data assimilation will
174 down-weight these differences if they occur in the presence of more internally consistent signals

175 from other proxies. Second, data assimilation allows us to overcome problems associated with
176 spatial bias in the proxy distribution (c.f., Fig. 1). Unlike the enhanced Younger Dryas cooling
177 shown by the proxy only curves (Fig. 4), LGMR reveals that Younger Dryas cooling was in fact
178 confined to the Northern Hemisphere (and, specifically, the North Atlantic and North Pacific sec-
179 tors; Extended Data Figure 7). The stronger expression of the YD in the proxy-only GMST curves
180 likely reflects the Northern Hemisphere bias in the underlying proxy distribution (Fig. 1a).

181 **Holocene global temperature trends**

182 The LGMR provides an updated view of the “Holocene Temperature Conundrum”². All of the
183 proxy-only reconstructions—including SMC, Temp12K⁷, and ours—show a cooling trend that
184 begins at ~9.5–6.5 kyr BP and continues through the rest of the Holocene (Fig. 4b) which, as
185 shown previously^{2,8,15}, disagrees with TraCE-21k (Fig. 4b). In contrast, LGMR shows that GMST
186 was relatively stable from ~8 kyr BP to pre-industrial, and remains within <0.5°C of TraCE-21k
187 GMST anomalies for >90% of the Holocene (Fig. 4b). The “flat” Holocene trend in LGMR does
188 not come directly from the model prior; the 6 ka model simulations in particular are warmer than
189 the posterior solution (c.f., Extended Data Table 2 and Methods). Rather, it is a feature of the
190 assimilation. Disagreement between proxy types, including the early Holocene warming in Mg/Ca
191 and $U_{37}^{K'}$ that underlies the Conundrum, is nearly eliminated after assimilating each into iCESM
192 (Extended Data Figure 6). Such consistency implies that a cold early Holocene and stable mid-
193 late Holocene is the most dynamically consistent and robust solution. Notably, this solution is not
194 exactly the same as the temperature evolution in TraCE-21k (Fig. 4b). LGMR indicates warmer
195 GMST from 9–5 kyr, reflecting warming in the high northern latitudes and the Southern Ocean
196 (Fig. 2). This suggests either seasonal rectification processes taking place in the climate system
197 that are underrepresented in models^{2,16,17}, or other deficiencies in TraCE-21k.

198 Recently, Bova et al.⁸ suggested that proxy-based Holocene cooling^{6,7} reflects orbitally
199 induced seasonal biases. Using a detrended compilation of Mg/Ca and $U_{37}^{K'}$ records, these authors

200 produced a SST reconstruction between 40°S and 40°N that shows a steady Holocene SST warm-
201 ing of ca. 0.5°C during the last 10 ka. Average LGMR SSTs from 40°S and 40°N are very similar
202 (Fig. 4b); however, we did not detrend any data. Rather, we use proxy forward models that account
203 for seasonal growth where this is expected on a first-principles basis ^{20–22}, which effectively miti-
204 gates the influence of seasonal bias on Holocene temperature evolution. However, LGMR further
205 shows that Holocene warming is in fact subdued once the high latitudes—which are warmer in the
206 early and mid-Holocene—are taken into account (Figs. 2-3). When global land areas are further
207 considered, the Holocene temperature trajectory is nearly flat (Fig. 4). This highlights the im-
208 portance of considering the full global land and ocean area when inferring global trends—a clear
209 strength of the LGMR over existing proxy-only methods.

210 Finally, the LGMR allows us to directly assess 20th and 21st century warming from the
211 broader vantage point of the past 24 ka. When juxtaposed alongside the Last Millennium Reanaly-
212 sis version 2.1 (also a paleoclimate data assimilation product; ¹⁸) and observational HadCRUT5 ¹¹
213 GMST (Fig. 2), we find that 2010–2019 mean GMST exceeds the upper bound (99th percentile) of
214 decadal-estimated values from the LGMR by a considerable margin— >0.5°C, or +1.4°C above
215 mean Holocene GMST. These findings contradict those of Marcott et al. ⁶, who suggested that early
216 21st century temperatures (2000–2009) had not yet exceeded early Holocene values and reflect in-
217 creased confidence over ref. ⁷, who find that 2010–2019 warming is at the ~80% of mid-Holocene
218 centennial-scale values. Similarly, we find the HadCRUT5-observed rate of 20th to 21st century
219 warming (0.96°C per century) registers near the upper bound of LGMR deglacial warming rates
220 (i.e., >99.9th percentile, Extended Data Figure 8 and Methods). As such, the LGMR underscores
221 the dramatic nature of anthropogenic warming, whose magnitude and rate appears unprecedented
222 in the context of the last 24 ka.

223 **References**

- 224 1. Liu, Z. *et al.* Transient Simulation of Last Deglaciation with a New Mechanism for Bølling-
225 Allerød Warming. *Science* **325**, 310 LP – 314 (2009).
- 226 2. Liu, Z. *et al.* The Holocene temperature conundrum. *Proceedings of the National Academy of*
227 *Sciences* **111**, E3501 LP – E3505 (2014).
- 228 3. Shakun, J. D. *et al.* Global warming preceded by increasing carbon dioxide concentrations
229 during the last deglaciation. *Nature* **484**, 49–54 (2012).
- 230 4. Snyder, C. W. Evolution of global temperature over the past two million years. *Nature* **538**,
231 226–228 (2016).
- 232 5. Bereiter, B., Shackleton, S., Baggenstos, D., Kawamura, K. & Severinghaus, J. Mean global
233 ocean temperatures during the last glacial transition. *Nature* **553**, 39–44 (2018).
- 234 6. Marcott, S. A., Shakun, J. D., Clark, P. U. & Mix, A. C. A Reconstruction of Regional and
235 Global Temperature for the Past 11,300 Years. *Science* **339**, 1198 LP – 1201 (2013).
- 236 7. Kaufman, D. *et al.* Holocene global mean surface temperature, a multi-method reconstruction
237 approach. *Scientific Data* **7**, 201 (2020).
- 238 8. Bova, S., Rosenthal, Y., Liu, Z., Godad, S. P. & Yan, M. Seasonal origin of the thermal maxima
239 at the Holocene and the last interglacial. *Nature* **589**, 548–553 (2021).
- 240 9. Hakim, G. J. *et al.* The last millennium climate reanalysis project: Framework and first results.
241 *Journal of Geophysical Research: Atmospheres* **121**, 6745–6764 (2016).
- 242 10. Tierney, J. E. *et al.* Glacial cooling and climate sensitivity revisited. *Nature* **584**, 569–573
243 (2020).

- 244 11. Morice, C. P. *et al.* An updated assessment of near-surface temperature change from 1850:
245 the HadCRUT5 dataset. *Journal of Geophysical Research: Atmospheres* **126**, e2019JD032361
246 (2020).
- 247 12. He, F. *et al.* Northern Hemisphere forcing of Southern Hemisphere climate during the last
248 deglaciation. *Nature* **494**, 81–85 (2013).
- 249 13. Praetorius, S. K. *et al.* The role of Northeast Pacific meltwater events in deglacial climate
250 change. *Science Advances* **6**, eaay2915 (2020).
- 251 14. Walczak, M. H. *et al.* Phasing of millennial-scale climate variability in the Pacific and Atlantic
252 Oceans. *Science* **370**, 716 LP – 720 (2020).
- 253 15. Marsicek, J., Shuman, B. N., Bartlein, P. J., Shafer, S. L. & Brewer, S. Reconciling divergent
254 trends and millennial variations in Holocene temperatures. *Nature* **554**, 92–96 (2018).
- 255 16. Brierley, C. M. *et al.* Large-scale features and evaluation of the PMIP4-CMIP6 mid-Holocene
256 simulations. *Climate of the Past* **16**, 1847–1872 (2020).
- 257 17. Park, H.-S., Kim, S.-J., Stewart, A. L., Son, S.-W. & Seo, K.-H. Mid-Holocene Northern
258 Hemisphere warming driven by Arctic amplification. *Science Advances* **5**, eaax8203 (2019).
- 259 18. Tardif, R. *et al.* Last Millennium Reanalysis with an expanded proxy database and seasonal
260 proxy modeling. *Clim. Past* **15**, 1251–1273 (2019).
- 261 19. Tierney, J. E. & Tingley, M. P. A Bayesian, spatially-varying calibration model for the TEX86
262 proxy. *Geochimica et Cosmochimica Acta* **127**, 83–106 (2014).
- 263 20. Tierney, J. E. & Tingley, M. P. BAYSPLINE: A New Calibration for the Alkenone Paleother-
264 mometer. *Paleoceanography and Paleoclimatology* **33**, 281–301 (2018).

- 265 21. Malevich, S. B., Vetter, L. & Tierney, J. E. Global Core Top Calibration of $\delta^{18}\text{O}$ in Planktic
266 Foraminifera to Sea Surface Temperature. *Paleoceanography and Paleoclimatology* **34**, 1292–
267 1315 (2019).
- 268 22. Tierney, J. E., Malevich, S. B., Gray, W., Vetter, L. & Thirumalai, K. Bayesian Calibration of
269 the Mg/Ca Paleothermometer in Planktic Foraminifera. *Paleoceanography and Paleoclima-*
270 *tology* **34**, 2005–2030 (2019).
- 271 23. Brady, E. *et al.* The Connected Isotopic Water Cycle in the Community Earth System Model
272 Version 1. *Journal of Advances in Modeling Earth Systems* **11**, 2547–2566 (2019).
- 273 24. Clark, P. U. *et al.* Global climate evolution during the last deglaciation. *Proceedings of the*
274 *National Academy of Sciences* **109**, E1134 LP – E1142 (2012).
- 275 25. Shakun, J. D. & Carlson, A. E. A global perspective on Last Glacial Maximum to Holocene
276 climate change. *Quaternary Science Reviews* **29**, 1801–1816 (2010).
- 277 26. Köhler, P., Nehrbass-Ahles, C., Schmitt, J., Stocker, T. F. & Fischer, H. A 156kyr smoothed
278 history of the atmospheric greenhouse gases CO₂, CH₄, and N₂O and their radiative forcing.
279 *Earth Syst. Sci. Data* **9**, 363–387 (2017).
- 280 27. Braconnot, P. & Kageyama, M. Shortwave forcing and feedbacks in Last Glacial Maximum
281 and Mid-Holocene PMIP3 simulations. *Philosophical Transactions of the Royal Society A:*
282 *Mathematical, Physical and Engineering Sciences* **373**, 20140424 (2015).
- 283 28. Bagginstos, D. *et al.* Earth’s radiative imbalance from the Last Glacial Maximum to the
284 present. *Proceedings of the National Academy of Sciences* **116**, 14881 LP – 14886 (2019).
- 285 29. North, G. R., Bell, T. L., Cahalan, R. F. & Moeng, F. J. Sampling Errors in the Estimation of
286 Empirical Orthogonal Functions. *Monthly Weather Review* **110**, 699–706 (1982).

- 287 30. Berger, A. Long-Term Variations of Daily Insolation and Quaternary Climatic Changes. *Journal of Atmospheric Sciences* **35**, 2362–2367 (1978).
288
- 289 31. Huybers, P. & Denton, G. Antarctic temperature at orbital timescales controlled by local
290 summer duration. *Nature Geoscience* **1**, 787–792 (2008).
- 291 32. Imbrie, J. *et al.* On the Structure and Origin of Major Glaciation Cycles 1. Linear Responses
292 to Milankovitch Forcing. *Paleoceanography* **7**, 701–738 (1992).
- 293 33. McManus, J. F., Francois, R., Gherardi, J.-M., Keigwin, L. D. & Brown-Leger, S. Collapse
294 and rapid resumption of Atlantic meridional circulation linked to deglacial climate changes.
295 *Nature* **428**, 834–837 (2004).
- 296 34. Böhm, E. *et al.* Strong and deep Atlantic meridional overturning circulation during the last
297 glacial cycle. *Nature* **517**, 73–76 (2015).
- 298 35. Lippold, J. *et al.* Constraining the Variability of the Atlantic Meridional Overturning Circula-
299 tion During the Holocene. *Geophysical Research Letters* **46**, 11338–11346 (2019).
- 300 36. Pedro, J. B. *et al.* Beyond the bipolar seesaw: Toward a process understanding of interhemi-
301 spheric coupling. *Quaternary Science Reviews* **192**, 27–46 (2018).
- 302 37. Ritz, S. P., Stocker, T. F., Grimalt, J. O., Menviel, L. & Timmermann, A. Estimated strength
303 of the Atlantic overturning circulation during the last deglaciation. *Nature Geoscience* **6**, 208–
304 212 (2013).
- 305 38. Praetorius, S. K. *et al.* North Pacific deglacial hypoxic events linked to abrupt ocean warming.
306 *Nature* **527**, 362–366 (2015).
- 307 39. Peltier, W. R., Argus, D. F. & Drummond, R. Space geodesy constrains ice age terminal
308 deglaciation: The global ICE-6G_C (VM5a) model. *Journal of Geophysical Research: Solid*
309 *Earth* **120**, 450–487 (2015).

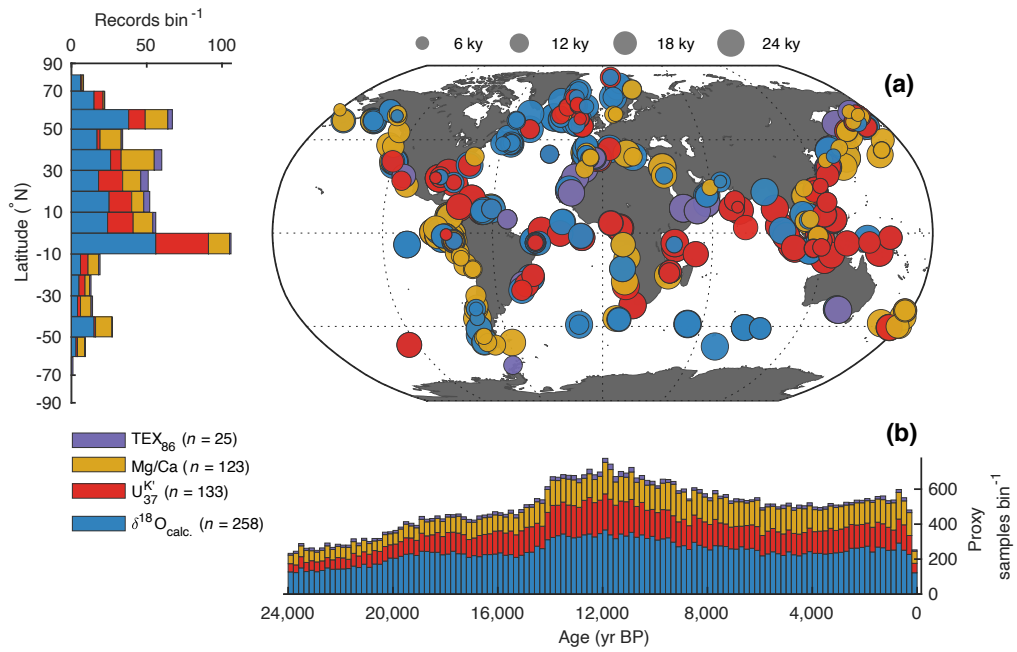


Fig. 1. Locations and temporal coverage of the SST proxies. (a) Site locations of TEX_{86} , Mg/Ca, $U_{37}^{K'}$ and $\delta^{18}\text{O}_{\text{calc.}}$ records (right), as well as their latitudinal distribution (left). (b) Temporal coverage of the proxies, binned at 200 yr intervals.

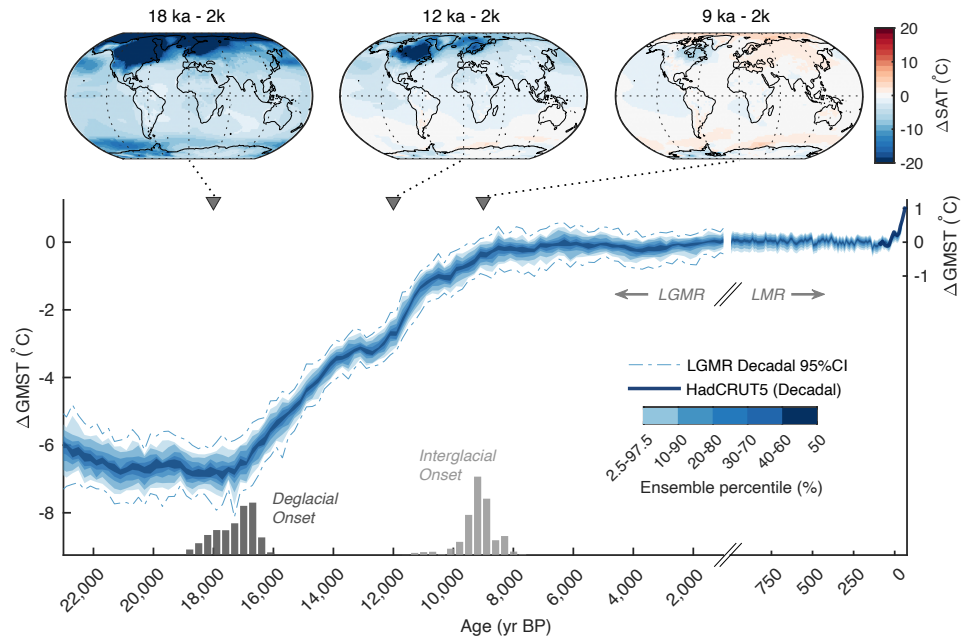


Fig. 2. Global mean surface temperature change over the last 24 ka. Ensemble distribution ($n = 300$) of LGMR GMST for the past 24 ka (blue colors), with a decadal 95th-percentile range (dotted-dashed lines) estimated using time-evolving GMST decadal-to-centennial mean ratios from iCESM (Methods). Shown at top are corresponding spatial surface temperature anomalies for intervals discussed in the main text. The estimated last deglacial and interglacial onset timings are shown as dark and light histograms at bottom (Methods). Juxtaposed alongside the LGMR (right-hand side) are reconstructed decadal GMST's from the Last Millennium Reanalysis v2.1¹⁸ and HadCRUT5 observational product¹¹. Δ GMST is computed relative to the pre-industrial last millennium average (1000-1850 CE).

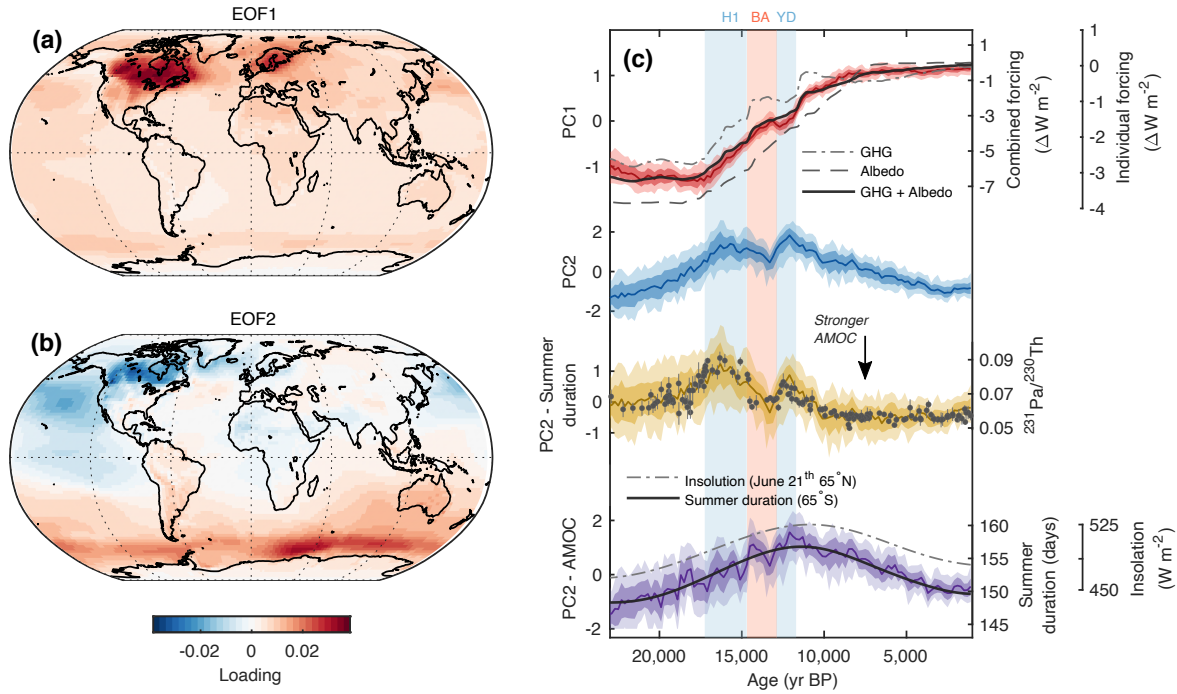


Fig. 3. Leading modes of LGM-to-present surface temperature variability. (a-b) Empirical orthogonal function (EOF) 1 and EOF2 of SAT during the last 24 ka. (c) Comparison between the associated principal component time series and climatic drivers. From top: PC1 (red) vs. greenhouse gas (GHG) radiative forcing²⁶, albedo radiative forcing (derived by scaling changes in ICE-6G-estimated global ice sheet area³⁹ to multi-model LGM global albedo forcing following ref.²⁸), and combined GHG and albedo radiative forcing; PC2 (blue); the residual of the regression of 65°S summer-duration onto PC2 (gold) vs. AMOC proxies from the Bermuda Rise ($^{231}\text{Pa}/^{230}\text{Th}$; error bars indicate 2σ uncertainty³⁵); and the residual of the regression of AMOC proxies onto PC2 (purple) vs. summer solstice 65°N insolation forcing³⁰ and 65°S summer-duration (the latter denoting the number of days where mean-annual insolation exceeds 250 W m^{-2} following³¹). All PC series are in normalized units. Dark and lighter shading on the time series indicate 1σ and 95% confidence intervals, respectively. Heinrich 1 (H1), the Bølling-Allerød (BA), and the Younger Dryas (YD) are also indicated.

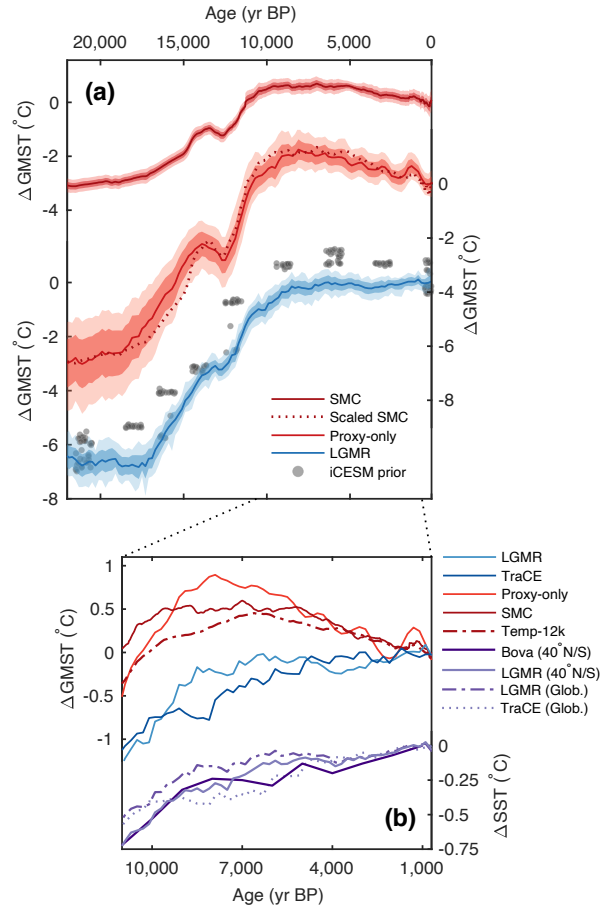


Fig. 4. Comparison of LGM-to-present surface temperature reconstructions. a) the SMC curve (dark red); proxy-only GMST (this study; light red), overlain with the GMST-scaled SMC curve (dotted dark red); and LGMR GMST (this study; blue). iCESM prior GMST values are shown in grey. Uncertainty ranges denote $\pm 1\sigma$ (dark) and 95% confidence intervals (light). (b) Holocene temperature trends from (a) differenced relative to the last millennium, alongside the Holocene reconstructions of ref. ⁷ (“Temp-12k”; red dotted-dashed), ref. ⁸ (“Bova”; dark purple), and TraCE-21k predictions ¹.

310 **Methods**

311 **Proxy compilation and screening** We collated a globally dispersed set of 573 sea surface temper-
312 ature (SST) proxy records spanning the past 24 thousand years before present (kyr BP). Following
313 ref. ¹⁰, we focus on geochemical proxies for SST including alkenone $U_{37}^{K'}$ (146 records), the
314 TetraEther indeX of 86 carbons (TEX₈₆; 28 records), the elemental ratio of Mg to Ca in planktic
315 foraminifera (Mg/Ca; 129 records), and the oxygen isotopic composition of planktic foraminifera
316 ($\delta^{18}O_c$; 270 records). As in ref. ¹⁰, we limit our analyses to these proxies because we have already
317 developed Bayesian forward models for each of them ^{19–22} that we can use in our paleoclimate
318 data assimilation scheme (see "Paleoclimate data assimilation", below). For consistency, we re-
319 calibrated all age models using the Marine13 radiocarbon calibration curve ⁴⁰ with the BACON
320 age model program ⁴¹. This procedure also allowed us to generate ensembles ($n = 1,000$) of pos-
321 sible age models for each record that were used to propagate dating uncertainties into our data
322 assimilation product (c.f. sections "Paleoclimate data assimilation" and "Proxy-only global mean
323 temperature" below).

324 Some screening of our proxy compilation was necessary to remove low resolution, short,
325 and adversely situated proxy records. Generally speaking, we removed records whose median age
326 resolution was less than 1,000 years and (or) were less than 4,000 years long (Extended Data Figure
327 1). However, this constraint was relaxed for records situated in or near the Southern Ocean, where
328 data coverage is sparse, so as to retain as many time series as possible from this undersampled
329 region. Next, to remove anomalous influences of sea ice on our proxy estimates (in particular, the
330 influence of sea ice on the $\delta^{18}O$ of seawater ²¹) we removed all records situated at locations where
331 pre-industrial mean annual SSTs were less than 0°C (a value assumed to roughly approximate the
332 perennial sea ice edge), as estimated from the World Ocean Atlas 2013 product ⁴². Following ref.
333 ²⁰, we omitted all $U_{37}^{K'}$ records situated north of 70°N or within the modern Arctic sea ice zone, due
334 to known biases in the alkenone temperature proxy that likely arise from lipid contributions from

335 Isochrysidales species living in sea ice ⁴³. We also removed two western Atlantic sites, OCE326-
336 GGC26 (43°29'N, 54°52'W) and OCE326-GGC30, (43°53'N, 62°48'W; ref. ⁴⁴). While these $U_{37}^{K'}$
337 records have been featured in prior mean global Holocene temperature reconstructions ⁶, they
338 show an extremely large (up to 10°C) cooling over the Holocene that most likely reflects a shift
339 in the Gulf Stream/Labrador Current boundary ⁴⁴. This poses a problem for our data assimilation
340 technique, because CESM1.2 does not put this sharp boundary in the same place as observations.
341 Assimilation of these sites thus has a tendency to cause a large regional bias in SSTs. All told, our
342 selection criteria resulted in the removal of 34 records.

343 **Proxy-only global mean temperature reconstruction** To provide a point of comparison for our
344 data assimilation results, we generated a reconstruction of global mean temperature change relative
345 to the pre-industrial using the screened (see above) proxy data, broadly following the methodology
346 of ref. ⁴⁵. This was done by first estimating a “reference” pre-industrial proxy value for each
347 site, and appending each value at the top of its respective $N \times 1$ proxy record. This produced
348 an $(N_i + 1) \times 1$ vector of proxy values for each site i , where the +1 denotes the appended pre-
349 industrial reference value. For sites with value(s) overlapping the last millennium (that is, 0–1
350 ky BP), the pre-industrial reference was computed as the last millennium mean proxy value. For
351 sites without last millennium overlap, pre-industrial reference proxy values were estimated by
352 using the nearest core-top value ^{19–22}. All $(N_i + 1) \times 1$ vectors were then calibrated to SSTs using
353 the Bayesian inverse models ^{19–22}. For the $\delta^{18}O_c$ and TEX_{86} models ^{20,21} we used prior standard
354 deviation values of 10°C, while for the $U_{37}^{K'}$ and Mg/Ca models ^{19,22} we used values of 5°C and
355 6°C, respectively. All prior standard deviation values are conservative, and only minimally impact
356 the posterior. The Mg/Ca model, BAYMAG, also requires constraints on salinity, pH, and bottom
357 water calcite saturation (Ω). The BAYMAG package includes functions to estimate past changes in
358 salinity and pH. Briefly, following refs. ²² and ⁴⁶, these functions scale the global sea level curve
359 ⁴⁷ to an inferred LGM global change of 1.1 psu, then add this to the modern mean annual value
360 of surface salinity for each site, as estimated from the World Ocean Atlas 2013 ⁴². Similarly, to

361 estimate changes in pH, BAYMAG scales the ice core $p\text{CO}_2$ record⁴⁸ to an inferred global increase
362 of 0.13 pH units during the LGM, and then adds this curve to the modern mean annual value of
363 surface pH estimated from the Global Ocean Data Analysis Project version 2 (GLODAPv2;⁴⁹).
364 Following ref.²², Ω is estimated at each records' bathymetric depth using the GLODAPv2 product
365 and assumed to be constant through time. The $\delta^{18}\text{O}_c$ model, BAYFOX, requires constraints on
366 the time-evolution of $\delta^{18}\text{O}$ of seawater. For this, we first scaled the benthic stack of ref.⁵⁰ to an
367 estimated change in global $\delta^{18}\text{O}$ of seawater (arising from changes in global ice volume) of $+1\text{‰}$
368 at the LGM (18 ka) relative to the pre-industrial following ref.⁵¹. This scaled curve was then
369 added to the modern mean annual $\delta^{18}\text{O}$ of seawater value⁵² and interpolated in time for each site.

370 The posterior SST estimates produced by the Bayesian inverse models are a matrix of di-
371 mension $(N_i + 1) \times M$, where M contains 1,000 possible SST histories and core-top reference
372 values for each time entry $N_i + 1$ of each i site. These matrices were sorted from least to greatest
373 along dimension M , which preserves the “shape” of the time series, after which a normally dis-
374 tributed analytical uncertainty of $\mathcal{N}(0, 0.5^\circ)$ was added back to the sorted ensembles to account
375 for laboratory precision (see also refs.¹⁰ and⁴⁵). Finally, we converted each of our records to SST
376 anomaly units relative to pre-industrial values (which we define as the last 1 ka mean for each site)
377 by subtracting the first row of the $(N_i + 1) \times M$ matrix (the pre-industrial core-top estimate) from
378 the remaining rows to generate an $N_i \times M$ matrix of SST anomalies.

379 In order to produce a global mean surface air temperature (GMST) anomaly curve, SST
380 anomaly values and associated ages were randomly drawn from our ensemble of M posterior
381 values and our ensemble of 1,000 age models, respectively, and then sorted into contiguous 200-yr
382 bins spanning back to 24 ka. If more than one data point per record occurred in a given 200 yr
383 bin, those SST data points were averaged, to ensure that higher-resolution records did not bias
384 the bin. Following refs.^{4,10} and⁵³, the data within each time bin were binned by latitude, with
385 the bin size randomly selected between 2.5 and 20°, and then global average SST (GSST) was

386 computed as the latitudinally weighted zonal average. Following ref. ⁵, GSST was then scaled
387 by a value randomly chosen between 1.96 and 2.92 to transform the values to GMST. This Monte
388 Carlo process was repeated 10,000 times, to propagate errors arising from the SST estimation, age
389 modeling, latitudinal weighting, and GSST to GMST scaling.

390 **Climate model simulations** The climate model priors are drawn from newly developed and pre-
391 existing climate simulations with the water isotope-enabled Community Earth System Model, ver-
392 sions 1.2 and 1.3 (iCESM1.2 and iCESM1.3). CESM1.2 is an updated version of CESM1 ⁵⁴, and
393 CESM1.3 contains further updates to the gravity wave scheme, cloud microphysics, and radiation
394 ⁵⁵. Critical for our purposes, iCESM explicitly simulates the transport and transformation of stable
395 water isotopes (e.g. H₂¹⁸O, HDO) in all of the component models, and has been shown to reproduce
396 key features of climate and isotopes in present-day and paleoclimate observations ²³. All of the
397 iCESM simulations have a horizontal resolution of 1.9 × 2.5° (latitude × longitude) in the atmo-
398 sphere and land, and a nominal 1° in the ocean. Preexisting iCESM simulations used in this study
399 include the pre-industrial and LGM simulations with iCESM1.3 ⁵⁶, the pre-industrial, 3 ka, 18 ka,
400 and LGM simulations with iCESM1.2 ¹⁰, and the Last Millennium simulation with iCESM1.2 ⁵⁷
401 (Extended Data Table 1).

402 In addition, we developed new time-slice simulations using iCESM1.2 of 16, 14, 12, 9, and 6
403 ka before present (Extended Data Table 1). For each time slice, the greenhouse gases (CO₂, CH₄,
404 and N₂O) were set to 200-year averages centered around the corresponding time from ice core
405 reconstructions ^{58–60}. Orbital parameters followed ³⁰. Ice sheet forcing was prescribed accord-
406 ing to the ICE-6G reconstruction ³⁹, including effects from changes in land elevation and surface
407 properties and the land-sea mask due to sea-level variations. For each time-slice simulation, ocean
408 temperature and salinity were initialized from published CESM1.2 simulations when available ⁶¹.
409 Seawater δ¹⁸O (δ¹⁸O_{sw}) was initialized from the slice before, e.g. δ¹⁸O_{sw} of 18 ka branched from
410 21 ka. A spatially uniform correction was applied to salinity and δ¹⁸O_{sw} to account for the ice-

411 volume effect. The correction terms were derived by scaling changes in the global volume-mean
412 salinity and $\delta^{18}\text{O}_{sw}$ between 21 and 0 ka by the corresponding change in the global mean sea level
413 ⁴⁷. Global volume-mean salinity and $\delta^{18}\text{O}_{sw}$ were 34.7 and 35.7 g kg⁻¹ and 0.05 and 1.05‰ in the
414 0 and 21 ka simulations, respectively ⁶². The iCESM1.2 time-slice simulations used pre-industrial
415 aerosol emissions because of the lack of reliable global reconstructions ⁶³. For a similar reason, the
416 simulations used the pre-industrial vegetation cover except for the 9 and 6 ka slices (see description
417 below). All these time-slice simulations were run for 900 years.

418 A “Green Sahara” was implemented in both the 9 and 6 ka simulations by prescribing a 100%
419 spatial coverage of shrub and C4 grass at 10–25°N and 25–35°N, respectively. In addition, C3 grass
420 over the Northern Hemisphere high latitude regions (northward of 50°N) was replaced with boreal
421 tree in the 6 ka simulation. These vegetation changes were developed following recommenda-
422 tions from the Paleoclimate Modeling Intercomparison Project and represent maximum possible
423 vegetation expansion over the Sahara and the Northern Hemisphere according to the pollen and
424 macro-fossil evidence ⁶⁴. To sample the uncertainty from vegetation, an additional 6 ka simulation
425 was performed for 400 years with the pre-industrial vegetation cover, as another end-member of
426 the mid-Holocene vegetation forcing. All the iCESM1.2 time slice simulations were run with a
427 prescribed satellite phenology in the land model due to the overall poor simulation of vegetation
428 processes with a prognostic phenology ⁶⁵. The satellite observation-derived vegetation phenology
429 included leaf area and stem area indices, and vegetation heights.

430 In addition, two water hosing experiments were performed within the 16 and 12 ka slices,
431 respectively, to provide prior climate states for the millennial-scale events of the last deglaciation
432 (i.e., Heinrich 1 and the Younger Dryas). In the hosing experiments, 0.25 Sv of freshwater with a
433 $\delta^{18}\text{O}$ composition of -30‰ (VSMOW) were applied over the northern North Atlantic (50–70°N).
434 These experiments were run for 200 years. Prior to using the simulations in our data assimilation,
435 a paleoclimate calendar adjustment was applied to the monthly model output for all time slices to

436 account for the effect of changing months on seasonal climatic expressions ⁶⁶.

437 **Paleoclimate data assimilation** The data assimilation method incorporates an offline ensemble
438 square root Kalman Filter approach, following the methodology of ref. ¹⁰ using the data assimilation
439 Matlab code package DASH version 3.6.1 (source code available at <https://github.com/JonKing93/DASH>). We refer the reader to this previous work for a full mathematical de-
440 scription. Briefly, the method combines a set of prior climate states from our model simulations
441 (X_{prior}) with new information from the proxy observations (the “innovation”, $Y_{obs} - Y_{est}$) to com-
442 pute a “posterior” matrix of assimilated past climate states, X_{post} , using the following Kalman
443 filter update equation:
444

$$X_{post} = X_{prior} + K(Y_{obs} - Y_{est}). \quad (1)$$

445 X_{prior} is a $N \times M$ matrix of prior climate states from iCESM, where dimension N contains the
446 model grid point data for SST and SSS (both at monthly and mean-annual resolution), and mean-
447 annual surface air temperature (SAT), $\delta^{18}\text{O}$ of surface seawater ($\delta^{18}\text{O}_{sw}$), precipitation amount-
448 weighted $\delta^{18}\text{O}$ ($\delta^{18}\text{O}_p$), and mean-annual precipitation rate collapsed into a concatenated vertical
449 “state vector,” and dimension M represents the number of state vector ensemble members.

450 The $P \times M$ matrix Y_{obs} consists of P globally dispersed $\delta^{18}\text{O}_c$, Mg/Ca, $U_{37}^{K'}$, and TEX₈₆
451 proxy observations, repeated column-wise M times for tractability. The matrix Y_{est} contains the
452 corresponding set of P proxy estimates, generated from the model output from each M state using
453 our Bayesian forward models. For details concerning the Bayesian models, the readers are referred
454 to the original publications ^{19–22}. In brief, the forward model for $\delta^{18}\text{O}_c$ requires monthly SST and
455 mean annual $\delta^{18}\text{O}_{sw}$. These $\delta^{18}\text{O}_c$ values are computed on a species- and growing season-specific
456 basis ²¹ that allows us to explicitly account for foraminiferal seasonal preferences in our forward
457 model proxy estimates. Both the $U_{37}^{K'}$ and TEX₈₆ models require only SST as inputs, with the
458 former requiring monthly SST due to the seasonal response of $U_{37}^{K'}$ production in the North Pacific,
459 the North Atlantic, and the Mediterranean ²⁰, and the latter only mean annual SST ¹⁹. Finally, the

460 forward model for Mg/Ca requires both monthly SST and SSS to compute species-specific growing
 461 season Mg/Ca values, in addition to sea-surface pH, bottom water calcite saturation state (Ω), and
 462 the laboratory cleaning method. The latter is provided in the original publications, and SST and
 463 SSS are drawn from iCESM output. For pH and Ω , we follow the same procedure as the proxy-only
 464 reconstruction (described above).

465 The innovation ($Y_{obs}-Y_{est}$) represents the new information from the observations not already
 466 provided by the prior estimates. As shown in Eq. (1), these values are weighted by the $N \times P$
 467 matrix K , the Kalman gain, which takes the general form:

$$K = cov(X_{prior}, Y_{est}) * [cov(Y_{est}, Y_{est}) + R]^{-1} \quad (2)$$

468 where “*cov*” denotes the covariance expectation. The $P \times P$ matrix R prescribes the error
 469 covariance associated with each proxy observation. Thus, the Kalman gain weights the innovation
 470 by the covariance of the forward-modeled proxy estimates with the prior climate states and the
 471 uncertainties of the prior-estimated proxy ensemble and the proxy observations. In our case, R is
 472 diagonal; i.e., the errors are presumed to be independent. R is user-defined, but ideally based on
 473 an estimate of “true” proxy uncertainties. Following ¹⁰, who systematically tested in the impact of
 474 different values of R on the posterior, we use the error values output from our Bayesian forward
 475 models scaled by 1/5, but further refine this by specifying a slightly different scaling factor for each
 476 proxy type. To determine these proxy-specific factors, for each record we performed jack-knife
 477 (leave one record out) and “only-one record” assimilation experiments (no R scalings applied) in
 478 order to assess the ability of any particular record to predict all others when that record was either
 479 removed, or solely retained, respectively. From these experiments, we then ranked each record by
 480 validating the only-one and all-but-one reconstructions against the non-assimilated proxies. This
 481 allowed assessment for the percent of tests for which this proxy resulted in “improvement” (as
 482 denoted by the ratio of the posterior to prior squared error of all predicted, independent proxies,

483 where a ratio less than unity indicates improvement). Using these rankings for each proxy type,
484 we then weighted each proxy-specific scaling factor by the improvement factor, and subsequently
485 weighted these rankings by total record count to maintain an average R -scaling of 1/5 across all
486 available proxy records. The specific scaling factors that we calculated were $r_{uk} = 3.13^{-1}$, $r_{tex} =$
487 1.36^{-1} , $r_{mgca} = 2.86^{-1}$, and $r_{18o} = 7.27^{-1}$, indicating $\delta^{18}\text{O}_c$ to be the most reliable (and numerous)
488 proxy type.

489 Following refs. ¹⁰ and ¹⁸, we applied covariance localization to the assimilation to limit
490 spurious relationships between proxies and far-field regions. Validation testing suggested that a
491 24,000 km localization radius provided optimal posterior results for our dataset (see “Internal and
492 external validation testing” below). This differs from ref. ¹⁰, who used a more narrow 12,000 km
493 localization. The improvement we find using broader localization likely relates to the fact that
494 fewer proxies are assimilated here per time step than in ref. ¹⁰.

495 For computing our full 24 kyr “Last Glacial Maximum Reanalysis” (LGMR) product, we
496 calculated X_{post} at 200-year increments using the following approach. First, we selected 80% of
497 our proxy records at random for inclusion in our assimilation, with the remaining 20% of records
498 withheld for statistical validation (see “Internal and external validation testing” below). For each
499 record, we randomly prescribed an age scale by drawing from the 1,000 viable posterior BACON-
500 derived age models. Second, for each 200-year interval, Y_{obs} was compiled as all of the available
501 proxy data points whose ages are within the bounds of the current reconstruction age-interval.
502 When multiple data points from a single record occurred within a given 200-year age-interval,
503 these values were averaged. We then randomly selected $M = 60$ state vector ensembles from the
504 iCESM output using a transient “evolving prior” approach (see below), and used the Bayesian
505 forward models to produce the matrix Y_{est} . X_{post} was then computed from Y_{obs} and Y_{est} (Eq. 1)
506 with R in the Kalman gain (Eq. 2) scaled to the appropriate proxy type. Finally, this process
507 was repeated for a total 300 times for each time interval, to create a 300-member LGM-to-present

508 ensemble of posterior states. This Monte Carlo procedure ensures that proxy, age-model, and
509 model prior uncertainties are included in the assimilated product. Since the age model uncertainties
510 in particular can be on the order of centuries, this sampling procedure has the effect of smoothing
511 the posterior time series on sub-millennial timescales.

512 Assimilation of the LGM-to-present climate evolution at 200-year intervals directly reflects
513 our underlying proxy data compilation. $\sim 96\%$ of the proxy records have a median resolution that
514 is higher than 200 years (Extended Data Figure 1). However, if all $>60,000$ compiled data points
515 are considered together, $>90\%$ of the paleoclimate data have sample resolutions of ≤ 200 years.
516 While ideally, the amount of time represented by the model prior would also equal 200 years,
517 this would have considerably limited the number of model priors available (a maximum of 58
518 prior states across our all iCESM time-slice simulations, and as few as 4 priors for a given interval;
519 Extended Data Table 1). In order to increase the number of iCESM priors available for assimilating
520 our marine proxies while still roughly adhering to our reconstruction interval, we instead used 50-
521 year average priors, following ref. ¹⁰. Prior experimentation by ref. ¹⁰ showed only marginal
522 differences in LGM and pre-industrial posteriors once time-averaging of our iCESM prior fields
523 exceed interannual time periods, justifying this choice.

524 Assimilating Earth's transient climate evolution between two fundamentally different glacial
525 versus interglacial states presents a unique obstacle for offline paleoclimate data assimilation
526 (which has largely focused on reconstructing the climate evolution of the Common Era ¹⁸, a rel-
527 atively stable background climate state ⁹). In terms of Bayesian inference, the challenge is ade-
528 quately assigning a collection of iCESM priors at each LGM-to-present reconstruction interval that
529 reflects a reasonable prior belief in their viability. For example, a time interval in the late Holocene
530 should not include glacial prior states that contain a Laurentide ice sheet, as the latter induces
531 fundamental changes in spatial covariance that are not realistic for a deglaciated climate state.
532 Conversely, deglacial prior states might include a range of possible Laurentide configurations.

533 To address this issue, we developed an “evolving prior” approach. For each 200-yr interval,
534 we defined a Normal probability density function (PDF) with a 1σ range of 4,000 years and a
535 maximum cutoff range of 3σ ($\pm 12,000$ years). The PDF is truncated to the range of our target time
536 interval (24–0 ka), such that for the tail ends of the reconstruction interval, the PDF ends up being
537 half-Normal. We then sampled 60 prior ages from this PDF and rounded them to 0, 3, 6, 9, 12,
538 14, 16, 18, or 21 ka BP, the discrete time-slice intervals at which iCESM simulations are available
539 (Extended Data Table 1). For each randomly drawn and rounded age, a model prior was selected
540 (with replacement) from its corresponding iCESM time-slice simulation.

541 The 1σ range of 4,000 years was chosen to balance the need to include adequate variability
542 in the prior while still excluding model priors that are not physically justified (i.e., the inclusion
543 of LGM priors when assimilating mid-late Holocene climatic states, and vice-versa). Validation
544 testing further indicated that this length scale was near-optimal, and also results in substantial
545 improvement over an “agnostic” prior sampling scheme (e.g., one that assigns equal probability of
546 including a prior from any given iCESM timeslice; see “Internal and external validation testing”,
547 below).

548 **Internal and external validation testing** Statistical validation and tuning of our LGMR prod-
549 uct was conducted in two ways, referred hereafter as “internal” and “external” validation. The
550 first approach (“internal” validation) involves withholding 20% of the marine proxies per iteration
551 (see “Paleoclimate data assimilation”, above), and then using the posterior SST, SSS, and $\delta^{18}\text{O}_{sw}$
552 fields to forward model the withheld proxy records. These predicted proxy records were then com-
553 pared with the actual proxy records using standard skill diagnostics: the coefficient of efficacy
554 (CE; a value between $-\infty$ and 1, where a value >0 is conventionally taken to represent skill over
555 climatology), the squared product moment coefficient (R^2), and the root mean square error of pre-
556 diction ($RMSEP$). The computation of multiple posterior ensembles (i.e., $N = 300$), each with
557 20% withholding, implies each proxy record was randomly withheld and internally validated on

558 average 60 times. These tests yield, on average, CE values that are greater than 0 with no obvi-
559 ous signs of systematic spatial biasing, indicative of skill in our posterior assimilation above our
560 evolving iCESM prior fields. On a global basis all posterior-predicted proxies exhibit a strong cor-
561 respondence to observed values with $R^2 > 0.95$ and slopes within 5% of their respective 1:1 lines
562 (Extended Data Figure 2), indicating a lack of systematic bias in the LGMR oceanic climatologies.

563 Following ref. ¹⁰, we also use independent ice core and speleothem records of $\delta^{18}\text{O}_p$ to
564 externally validate the LGMR. In this more stringent analysis, we compare posterior $\delta^{18}\text{O}_p$ to
565 published ice core $\delta^{18}\text{O}$ (which is taken as a direct indicator of precipitation-weighted mean-annual
566 $\delta^{18}\text{O}_p$, given that post-depositional processes such as isotopic diffusion ⁶⁷ and sublimation ⁶⁸ do not
567 typically impact ice core record integrity across centennial and longer time scales) and speleothem
568 $\delta^{18}\text{O}$, which is first converted to $\delta^{18}\text{O}_p$ via the methodology of ref. ⁶⁹ (see also ref. ¹⁰). For
569 the speleothem data, we used the SISAL version 1b database ⁷⁰. Records were included in our
570 compilation solely on the basis that they span at least 18,000 years: that is, at least three-quarters
571 of the LGMR reconstruction interval, ensuring overlap with the deglacial period (ca. 17–9 ka;
572 Fig. 2). Record-specific details are provided in Extended Data Table 2. Following ref. ¹⁰, we
573 focus on $\delta^{18}\text{O}_p$ deviations ($\Delta\delta^{18}\text{O}_p$), which we generate by differencing all $\delta^{18}\text{O}_p$ values at each
574 time slice interval relative to the 0 ka baseline. This approach is premised on the expectation that
575 $\delta^{18}\text{O}_p$ deviations should be adequately captured by LGMR ¹⁰ despite known mean $\delta^{18}\text{O}_p$ biases
576 in iCESM ²³. We then compare both prior and posterior $\Delta\delta^{18}\text{O}_p$ with observed $\Delta\delta^{18}\text{O}_p$ at the
577 iCESM timeslice intervals (3, 6, 9, 12, 14, 16, 18, and 21 ka BP) using our statistical diagnostics
578 of covariance and prediction error (R^2 and $RMSEP$). Positive ΔR^2 (i.e., a stronger relationship
579 with observed values in LGMR vs. the prior) and negative $\Delta RMSEP$ (i.e., reduced prediction
580 error in LGMR vs. the prior) imply improvement in our LGMR posterior relative to the iCESM
581 priors.

582 Overall, this external validation test indicates that LGMR substantially improves over the

583 prior, with a nearly 30% error reduction ($RMSEP_{prior} = 2.60\%$; $RMSEP_{posterior} = 1.91\%$) and
584 approaching $2\times$ greater variance explained in with our posterior-predicted values relative to the
585 prior ($R_{prior}^2 = 0.37$; $R_{posterior}^2 = 0.62$). Although much of the improvement is driven by ice core
586 $\Delta\delta^{18}\text{O}_p$ estimates (Extended Data Figure 3 and Extended Data Figure 4), offsets with speleothem
587 $\Delta\delta^{18}\text{O}_p$ observations are also strongly reduced in LGMR relative to iCESM. The comparably poor
588 temporal covariance shown by global speleothem $\Delta\delta^{18}\text{O}_p$ values relative to ice cores (Extended
589 Data Figure 4; Extended Data Table 2) may reflect local-scale influences on speleothem $\delta^{18}\text{O}_p$
590 records, such as groundwater storage, mixing, recharge, and residence time variations; subgrid-
591 scale topographic and (or) precipitation influences; and uncertainties arising from indirectly infer-
592 ring $\delta^{18}\text{O}_p$ from $\delta^{18}\text{O}_{calcite}$ or $\delta^{18}\text{O}_{aragonite}$ measurements⁶⁹. In addition, the iCESM prior range
593 of $\delta^{18}\text{O}_p$ across the LGM to present in the tropics is considerably smaller than in the high latitudes
594 (e.g., Extended Data Figure 4), which might restrict the posterior solutions for the speleothems
595 (c.f. ref.¹⁰).

596 We used external validation testing to choose both the covariance localization radius and
597 evolving prior 1σ range (see "Paleoclimate data assimilation" for description of each). Between
598 the two, our tests show that LGMR is most sensitive to the choice of localization radius. We tested
599 values between 6,000 and infinite (i.e., no localization) km and found a relatively broad localization
600 cutoff (24,000 km) is near-optimal (Extended Data Table 3). In contrast, LGMR shows comparably
601 less sensitivity to choice of the 1σ range for sampling iCESM priors, with acceptable external
602 validation scoring for values between $1\sigma = 2,000\text{--}6,000$ years (Extended Data Table 3). For our
603 final LGMR product we chose a value of $1\sigma = 4000$ years as this was shown to provide near-
604 optimal validation scoring (Extended Data Table 3), while also constituting a reasonable "middle
605 ground" between enabling adequate variance amongst iCESM model priors throughout the last 24
606 kyr while excluding physically unjustifiable states (see discussion above).

607 **Proxy specific reconstructions** We assess the influence of each proxy type on our results by
608 conducting proxy-specific reconstructions of LGM-to-present GMST using both our “proxy-only”
609 (see, “Proxy only global mean temperature reconstruction”, above) as well as data assimilation
610 (see, “Paleoclimate data assimilation”, above) approaches. Due to the limited number of TEX₈₆
611 records (28), our analysis is focused on $U_{37}^{K'}$, Mg/Ca, and $\delta^{18}O_c$. Overall, we find that GMSTs
612 are, on average, mildly warmer in our proxy-only reconstructions than in our data assimilation
613 results across all proxy types, a difference that is especially pronounced during the early Holocene
614 (ca 9–8 ka) period (Extended Data Figure 6). Uncertainties are largest for the proxy-only Mg/Ca
615 reconstruction, which appears to be the least internally consistent of the six reconstructions (Ex-
616 tended Data Figure 6c) implying that it is the least reliable proxy type. Most likely, this reflects
617 the multivariate sensitivity of this proxy. In particular, since our iCESM simulations do not in-
618 clude an interactive ocean carbon cycle, we make basic assumptions about surface water pH and
619 bottom water saturation to forward model Mg/Ca. Bottom water saturation (Ω) in particular is the
620 second-most important environmental influence on foraminiferal Mg/Ca after temperature²², and
621 must have changed dramatically across the deglacial transition. Unfortunately, we lack good con-
622 straints on Ω , so we must assume that it is constant through time. Despite these concerns, we do
623 not have probable cause nor reason to consider Mg/Ca inherently “incorrect,” and it is clear from
624 the proxy-specific experiments that data assimilation draws the Mg/Ca data closer to a solution
625 that is consistent with $U_{37}^{K'}$ and $\delta^{18}O_c$ (Extended Data Figure 6d).

626 The proxy-only Mg/Ca and $U_{37}^{K'}$ reconstructions show cooling across the Holocene since
627 about 8 ka (Extended Data Figure 6b and c), a feature that translates into the full proxy-only
628 reconstruction (Fig. 4a). However, these trends are eliminated after assimilating the same proxy
629 data with iCESM; for $U_{37}^{K'}$, the Holocene cooling trend switches entirely to Holocene warming
630 (Extended Data Figure 6b). Similarly, for $\delta^{18}O_c$ we find that the stable Holocene temperature
631 evolution implied by the proxy-only method becomes a warming trend when assimilated with
632 iCESM. Collectively, the consistency we observe amongst our data assimilated results implies a

633 cold early Holocene and stable mid-late Holocene is a dynamically consistent solution under the
634 confines of our underlying proxy-model covariance, a finding that is all the more remarkable given
635 that this isn't an obvious feature of our iCESM priors (Fig. 4a and Extended Data Figure 6).

636 **Timing of last deglacial and interglacial onset** We quantify the onset timing of the last deglacial
637 and current interglacial periods by considering GMST of the last 24 ka as a linearly contiguous
638 three part sequence: a glacial period, a deglacial period, and an interglacial period. We incorporate
639 the Bayesian changepoint methodology of ⁷¹ to isolate the two leading changepoints separating
640 these three periods, accounting for time and temperature uncertainty through Monte Carlo ran-
641 domization ($n = 10,000$). In each iteration, we produce a surrogate 24 ka GMST time series by
642 1) normal random sampling of temperature for each 200-yr interval, using the LMGR ensemble
643 mean and standard deviation and 2) uniform random sampling an associated age for each 200-yr
644 interval. For each resultant time- and temperature-perturbed global mean temperature time se-
645 ries, we then determine the location of the two changepoints; for each iteration, we assume that
646 the leading changepoint denotes the deglaciation onset and that the second changepoint denotes
647 the interglacial onset. This analysis indicates a deglaciation onset at 17.2 ka (18.7–16.4 ka 95%
648 confidence interval), and an interglacial onset at 9.2 (8.3–11.0) ka (Fig. 2).

649 **Contextualizing the rate and magnitude of modern warming** In order to compare the magni-
650 tude and rate of industrial-era warming (from the HadCRUT5 product ¹¹) to global temperature
651 changes estimated by LGMR, we first adjusted the LGMR and HadCRUT5 GMST anomalies to a
652 common, overlapping frame of reference. This was accomplished by re-centering GMST estimates
653 from the Last Millennium Reanalysis (LMR) v2.1 ¹⁸ as anomalies relative to 1000–1850 CE, and
654 then adjusting LGMR and HadCRUT5 to this LMR frame of reference during their respective over-
655 lapping periods: 1000–1950 CE for LGMR and 1850–2000 CE for HadCRUT5. Next, in order to
656 directly compare decadal-mean HadCRUT5 GMST values to LGMR GMST values, we adjusted
657 the latter (LGMR) for decadal-to-centennial variance attenuation. This was done by individually

658 scaling the LGMR GMST ensemble variance by the GMST decadal-to-centennial mean variance
659 ratio from iCESM at each reconstruction time interval using our evolving prior approach (see Fig.
660 2). This adjustment produces pseudo decadal-mean GMST values for all LGMR time-intervals,
661 rendering comparison to HadCRUT5 decadal-mean GMST more direct and conservative. Com-
662 parison between the decadal-adjusted LGMR and HadCRUT5 indicates that decadal mean GMST
663 exceeded the range ($>99^{th}$ percentile) of Holocene values by the turn of the 21st century (2000–
664 2009; Fig. 2). During the most recent decade (2010–2019), GMST exceeded maximum Holocene
665 values by a more considerable margin: $>0.5^{\circ}\text{C}$, corresponding to $+1.4^{\circ}\text{C}$ above mean Holocene
666 GMST.

667 To compare the centennial-scale rate of temperature change in LGMR to HadCRUT5, we
668 randomly sampled GMST ($n = 10,000$) from the decadal-adjusted LGMR for each time interval
669 across the deglaciation (ca. 17.2–9.2 ka; see “Timing of last deglacial and interglacial onset”,
670 above), which contains the largest and most rapid changes in GMST during the last 24 kyr (Fig.
671 2). These randomly sampled values of GMST were then used to estimate rates of change moving
672 forward in time across adjoining time intervals, allowing us to develop a large distribution of
673 possible deglacial warming rates. Our analysis shows that by the 20th century (1900–1999 CE),
674 the rate of industrial era warming ($0.72^{\circ}\text{C century}^{-1}$) exceeded the 99^{th} percentile of composited
675 warming rates for all time intervals of the deglaciation. In the ensuing (most-recent) two decades,
676 the rate of centennial-scale GMST warming has risen by an additional $\sim 36\%$ ($0.98^{\circ}\text{C century}^{-1}$ for
677 the period 1920–2019 CE; Extended Data Figure 8b), thus recently exceeding the 99^{th} percentile
678 of each individual reconstructed deglacial time interval (Extended Data Figure 8c).

Code availability The MATLAB code used for the reconstruction (DASH) are publicly available (<https://github.com/JonKing93/DASH>), as are all accompanying Bayesian proxy forward models (BAYSPAR, BAYSPLINE, BAYFOX, and BAYMAG) used in this study (<https://github.com/jesstierney>). The iCESM1.2 model code is available at <https://github.com>.

com/NCAR/iCESM1.2.

Data availability LGMR and associated proxy data will be made publicly available pending acceptance of this manuscript.

Methods References

40. Reimer, P. J. *et al.* IntCal13 and Marine13 Radiocarbon Age Calibration Curves 0–50,000 Years cal BP. *Radiocarbon* **55**, 1869–1887 (2013).
41. Blaauw, M. & Christen, J. A. Flexible paleoclimate age-depth models using an autoregressive gamma process. *Bayesian Anal.* **6**, 457–474 (2011).
42. Locarnini, R. A. *et al.* World ocean atlas 2013. Volume 1, Temperature (2013).
43. Wang, K. J. *et al.* Group 2i Isochrysidales produce characteristic alkenones reflecting sea ice distribution. *Nature Communications* **12**, 1–10 (2021).
44. Sachs, J. P. Cooling of Northwest Atlantic slope waters during the Holocene. *Geophysical Research Letters* **34** (2007).
45. Tierney, J. E., Haywood, A. M., Feng, R., Bhattacharya, T. & Otto-Bliesner, B. L. Pliocene Warmth Consistent With Greenhouse Gas Forcing. *Geophysical Research Letters* **46**, 9136–9144 (2019).
46. Gray, W. R. & Evans, D. Nonthermal Influences on Mg/Ca in Planktonic Foraminifera: A Review of Culture Studies and Application to the Last Glacial Maximum. *Paleoceanography and Paleoclimatology* **34**, 306–315 (2019).
47. Lambeck, K., Rouby, H., Purcell, A., Sun, Y. & Sambridge, M. Sea level and global ice volumes from the Last Glacial Maximum to the Holocene. *Proceedings of the National Academy of Sciences* **111**, 15296 LP – 15303 (2014).
48. Bereiter, B. *et al.* Revision of the EPICA Dome C CO₂ record from 800 to 600kyr before present. *Geophysical Research Letters* **42**, 542–549 (2015).
49. Olsen, A. *et al.* The Global Ocean Data Analysis Project version 2 (GLODAPv2) – an internally consistent data product for the world ocean. *Earth Syst. Sci. Data* **8**, 297–323 (2016).

50. Lisiecki, L. E. & Raymo, M. E. A Pliocene-Pleistocene stack of 57 globally distributed benthic $\delta^{18}\text{O}$ records. *Paleoceanography* **20** (2005).
51. Schrag, D. P., Hampt, G. & Murray, D. W. Pore Fluid Constraints on the Temperature and Oxygen Isotopic Composition of the Glacial Ocean. *Science* **272**, 1930 LP – 1932 (1996).
52. LeGrande, A. N. & Schmidt, G. A. Global gridded data set of the oxygen isotopic composition in seawater. *Geophysical Research Letters* **33** (2006).
53. Zhu, J., Poulsen, C. J. & Tierney, J. E. Simulation of Eocene extreme warmth and high climate sensitivity through cloud feedbacks. *Science advances* **5**, eaax1874 (2019).
54. Hurrell, J. W. *et al.* The Community Earth System Model: A Framework for Collaborative Research. *Bulletin of the American Meteorological Society* **94**, 1339–1360 (2013).
55. Meehl, G. A. *et al.* Effects of Model Resolution, Physics, and Coupling on Southern Hemisphere Storm Tracks in CESM1.3. *Geophysical Research Letters* **46**, 12408–12416 (2019).
56. Zhu, J. *et al.* Reduced ENSO variability at the LGM revealed by an isotope-enabled Earth system model. *Geophysical Research Letters* **44**, 6984–6992 (2017).
57. Stevenson, S. *et al.* Volcanic Eruption Signatures in the Isotope-Enabled Last Millennium Ensemble. *Paleoceanography and Paleoclimatology* **34**, 1534–1552 (2019).
58. Lüthi, D. *et al.* High-resolution carbon dioxide concentration record 650,000–800,000years before present. *Nature* **453**, 379–382 (2008).
59. Louergue, L. *et al.* Orbital and millennial-scale features of atmospheric CH_4 over the past 800,000years. *Nature* **453**, 383–386 (2008).
60. Schilt, A. *et al.* Atmospheric nitrous oxide during the last 140,000 years. *Earth and Planetary Science Letters* **300**, 33–43 (2010).

61. DiNezio, P. N. *et al.* Glacial changes in tropical climate amplified by the Indian Ocean. *Science Advances* **4**, eaat9658 (2018).
62. Duplessy, J.-C., Labeyrie, L. & Waelbroeck, C. Constraints on the ocean oxygen isotopic enrichment between the Last Glacial Maximum and the Holocene: Paleoceanographic implications. *Quaternary Science Reviews* **21**, 315–330 (2002).
63. Kageyama, M. *et al.* The pmip4 contribution to cmip6–part 4: Scientific objectives and experimental design of the pmip4-cmip6 last glacial maximum experiments and pmip4 sensitivity experiments. *Geoscientific Model Development* **10**, 4035–4055 (2017).
64. Otto-Bliesner, B. L. *et al.* The pmip4 contribution to cmip6–part 2: Two interglacials, scientific objective and experimental design for holocene and last interglacial simulations. *Geoscientific Model Development* **10**, 3979–4003 (2017).
65. Lawrence, D. M. *et al.* Parameterization improvements and functional and structural advances in Version 4 of the Community Land Model. *Journal of Advances in Modeling Earth Systems* **3** (2011).
66. Bartlein, P. J. & Shafer, S. L. Paleo calendar-effect adjustments in time-slice and transient climate-model simulations (PaleoCalAdjust v1.0): impact and strategies for data analysis. *Geosci. Model Dev.* **12**, 3889–3913 (2019).
67. Jones, T. R. *et al.* Water isotope diffusion in the WAIS Divide ice core during the Holocene and last glacial. *Journal of Geophysical Research: Earth Surface* **122**, 290–309 (2017).
68. Sokratov, S. A. & Golubev, V. N. Snow isotopic content change by sublimation. *Journal of Glaciology* **55**, 823–828 (2009).
69. Comas-Bru, L. *et al.* Evaluating model outputs using integrated global speleothem records of climate change since the last glacial. *Clim. Past* **15**, 1557–1579 (2019).

70. Atsawawaranunt, K. *et al.* The SISAL database: a global resource to document oxygen and carbon isotope records from speleothems. *Earth Syst. Sci. Data* **10**, 1687–1713 (2018).
71. Ruggieri, E. A Bayesian approach to detecting change points in climatic records. *International Journal of Climatology* **33**, 520–528 (2013).
72. Blunier, T. & Brook, E. J. Timing of Millennial-Scale Climate Change in Antarctica and Greenland During the Last Glacial Period. *Science* **291**, 109 LP – 112 (2001).
73. Stenni, B. *et al.* Expression of the bipolar see-saw in Antarctic climate records during the last deglaciation. *Nature Geoscience* **4**, 46–49 (2011).
74. Watanabe, O. *et al.* Homogeneous climate variability across East Antarctica over the past three glacial cycles. *Nature* **422**, 509–512 (2003).
75. Brook, E. J. *et al.* Timing of millennial-scale climate change at Siple Dome, West Antarctica, during the last glacial period. *Quaternary Science Reviews* **24**, 1333–1343 (2005).
76. Stenni, B. *et al.* The deuterium excess records of EPICA Dome C and Dronning Maud Land ice cores (East Antarctica). *Quaternary Science Reviews* **29**, 146–159 (2010).
77. Steig, E. J. *et al.* Synchronous Climate Changes in Antarctica and the North Atlantic. *Science* **282**, 92 LP – 95 (1998).
78. Petit, J. R. *et al.* Climate and atmospheric history of the past 420,000 years from the Vostok ice core, Antarctica. *Nature* **399**, 429–436 (1999).
79. Markle, B. R. *et al.* Global atmospheric teleconnections during Dansgaard–Oeschger events. *Nature Geoscience* **10**, 36–40 (2017).
80. Vinther, B. M. *et al.* Synchronizing ice cores from the Renland and Agassiz ice caps to the Greenland Ice Core Chronology. *Journal of Geophysical Research: Atmospheres* **113**, D08115 (2008).

81. Stuiver, M. & Grootes, P. M. GISP2 Oxygen Isotope Ratios. *Quaternary Research* **53**, 277–284 (2000).
82. Johnsen, S. J. *et al.* The $\delta^{18}\text{O}$ record along the Greenland Ice Core Project deep ice core and the problem of possible Eemian climatic instability. *Journal of Geophysical Research: Oceans* **102**, 26397–26410 (1997).
83. Andersen, K. K. *et al.* High-resolution record of Northern Hemisphere climate extending into the last interglacial period. *Nature* **431**, 147–151 (2004).
84. Holmgren, K. *et al.* Persistent millennial-scale climatic variability over the past 25,000 years in Southern Africa. *Quaternary Science Reviews* **22**, 2311–2326 (2003).
85. Novello, V. F. *et al.* Two Millennia of South Atlantic Convergence Zone Variability Reconstructed From Isotopic Proxies. *Geophysical Research Letters* **45**, 5045–5051 (2018).
86. Cheng, H. *et al.* The climate variability in northern Levant over the past 20,000 years. *Geophysical Research Letters* **42**, 8641–8650 (2015).
87. Dutt, S. *et al.* Abrupt changes in Indian summer monsoon strength during 33,800 to 5500 years B.P. *Geophysical Research Letters* **42**, 5526–5532 (2015).
88. Ayliffe, L. K. *et al.* Rapid interhemispheric climate links via the Australasian monsoon during the last deglaciation. *Nature Communications* **4**, 2908 (2013).
89. Partin, J. W., Cobb, K. M., Adkins, J. F., Clark, B. & Fernandez, D. P. Millennial-scale trends in west Pacific warm pool hydrology since the Last Glacial Maximum. *Nature* **449**, 452–455 (2007).
90. Cai, Y. *et al.* Variability of stalagmite-inferred Indian monsoon precipitation over the past 252,000 y. *Proceedings of the National Academy of Sciences* **112**, 2954–2959 (2015).

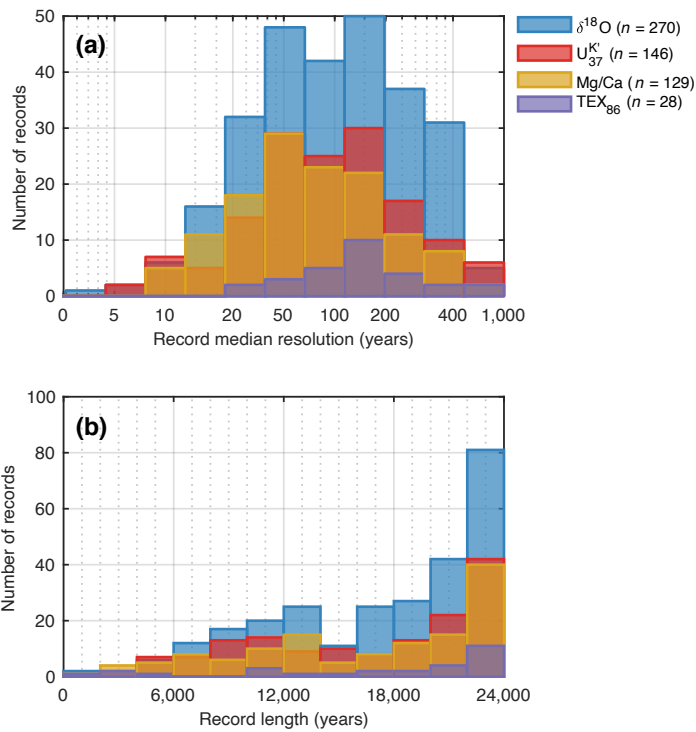
91. Fleitmann, D. *et al.* Timing and climatic impact of Greenland interstadials recorded in stalagmites from northern Turkey. *Geophysical Research Letters* **36**, L19707 (2009).
92. Cruz, F. W. *et al.* Insolation-driven changes in atmospheric circulation over the past 116,000 years in subtropical Brazil. *Nature* **434**, 63–66 (2005).
93. Hellstrom, J., McCulloch, M. & Stone, J. A Detailed 31,000-Year Record of Climate and Vegetation Change, from the Isotope Geochemistry of Two New Zealand Speleothems. *Quaternary Research* **50**, 167–178 (1998).
94. Grant, K. M. *et al.* Rapid coupling between ice volume and polar temperature over the past 150,000years. *Nature* **491**, 744–747 (2012).
95. Cheng, H. *et al.* Climate change patterns in Amazonia and biodiversity. *Nature Communications* **4**, 1411 (2013).

Acknowledgements We thank B. Malevich for early discussions and explorations on LGM-to-present data assimilation, and M. Fox and N. Rapp for help in compiling the proxy data. We thank P. DiNezio for providing initial and boundary condition files for the CESM simulations, and B. Markle for assistance in compiling and sharing the ice core water isotope data. This study was supported by National Science Foundation (NSF) grant numbers AGS-1602301 and AGS-1602223, and Heising-Simons Foundation grant numbers 2016-012, 2016-014, and 2016-015. The CESM project is supported primarily by the NSF. This material is based upon work supported by the National Center for Atmospheric Research, which is a major facility sponsored by the NSF under Cooperative Agreement No. 1852977. Computing and data storage resources, including the Cheyenne supercomputer (doi:10.5065/D6RX99HX), were provided by the Computational and Information Systems Laboratory (CISL) at NCAR.

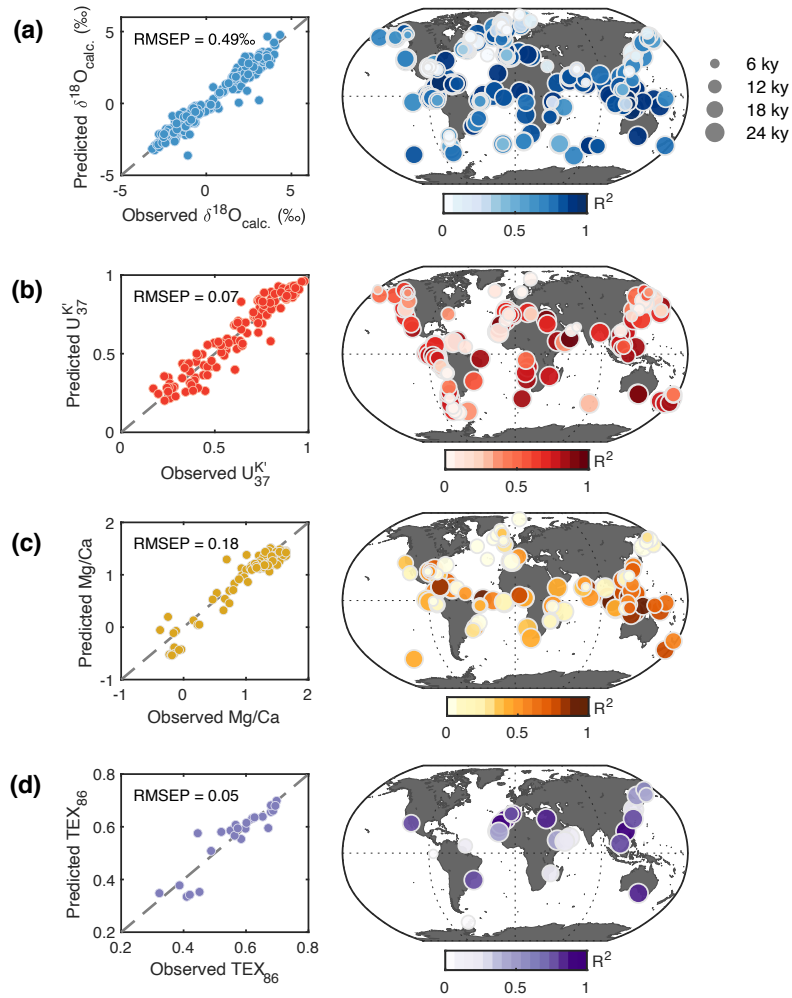
Author contributions M.B.O. conducted the data assimilation, led the analysis and interpretation of the results, and designed the figures. M.B.O. and J.E.T. led the writing of this paper. J.E.T. led the proxy data compilation. J.K. wrote the DASH code, based on methods and input by R.T. and G.J.H. J.Z. and C.J.P. planned and conducted the iCESM simulations. All authors contributed to the design of the study and the writing of this manuscript.

Competing interests The authors declare that they have no competing financial interests.

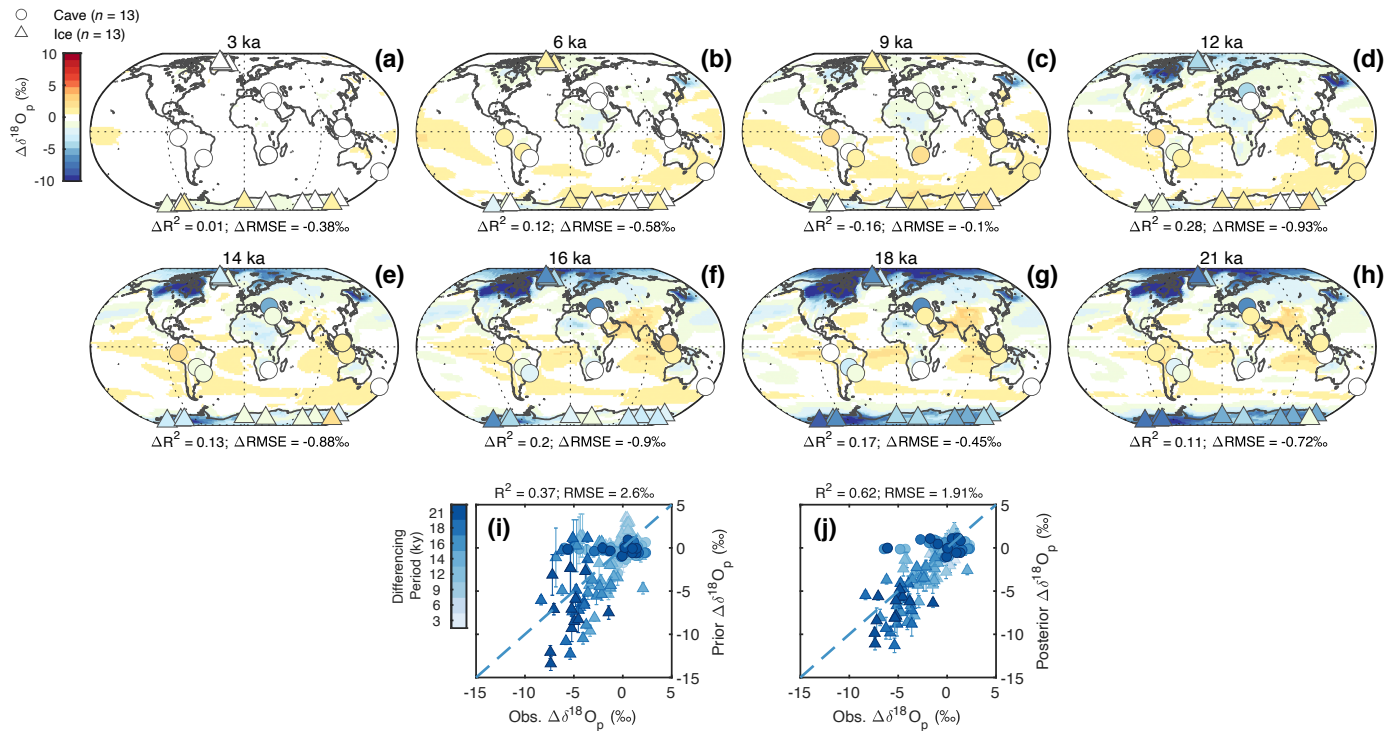
Correspondence Correspondence should be addressed to M.B.O. (mattosman@arizona.edu).



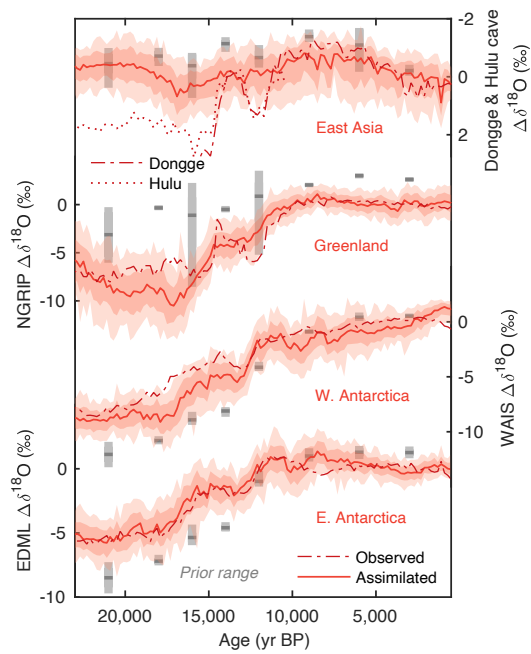
Extended Data Figure 1. Time resolution and temporal coverage of the SST proxy data compilation. (a). Histogram of record resolution (denoting the median sample resolution for each record), computed for each proxy type. (b) Histogram of record length for each proxy type.



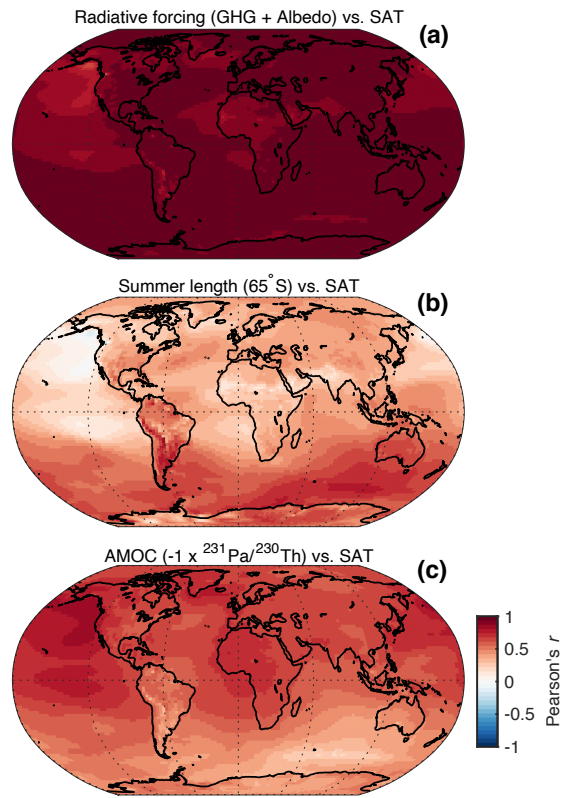
Extended Data Figure 2. Statistical validation of randomly withheld marine geochemical proxies. (a) From left: observed vs. forward-modeled $\delta^{18}\text{O}_c$ values for each site using the posterior data assimilation estimates. Shown at right are the associated median (based on $n = 300$ ensemble members) $R^2_{\text{validation}}$ scores, computed on a per-site basis. (b-d) As in (a), but for $U_{37}^{K'}$, Mg/Ca, and TEX_{86} , respectively.



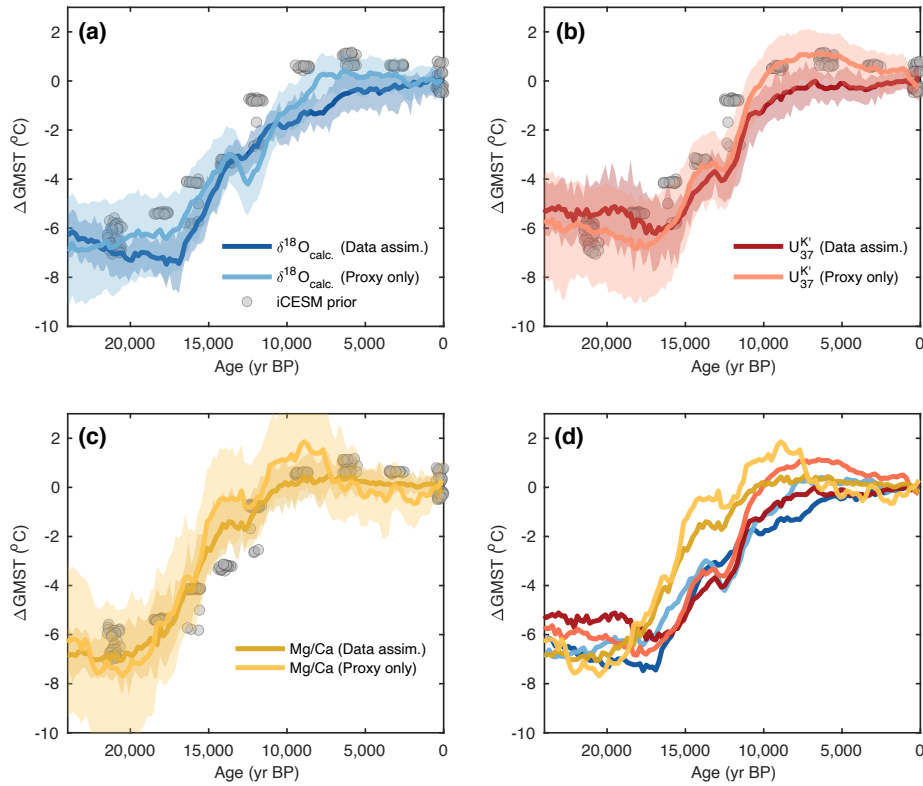
Extended Data Figure 3. Validation using independent $\delta^{18}O_p$ ice core and speleothem records. (a) 3 ka - preindustrial (PI) posterior $\Delta\delta^{18}O_p$ field; overlying dots show the observed 3 ka - PI $\Delta\delta^{18}O_p$ values from speleothems and ice cores. Only records spanning at least 18 of the last 24 ka are shown. ΔR^2 and $\Delta RMSEP$ values denote the change in observed vs. posterior assimilated $\Delta\delta^{18}O_p$ values relative to the prior (i.e., iCESM) estimated values. (b-h) As in (a), but for values differenced at 6, 9, 12, 14, 16, 18, and 21 ka vs. the PI, respectively. (i) All observed $\Delta\delta^{18}O_p$ vs. model prior values; dashed line indicates the 1:1 relationship. (j) All observed $\Delta\delta^{18}O_p$ vs. posteriors (a-h), which shows a strong improvement in ΔR^2 and $\Delta RMSEP$ over the prior.



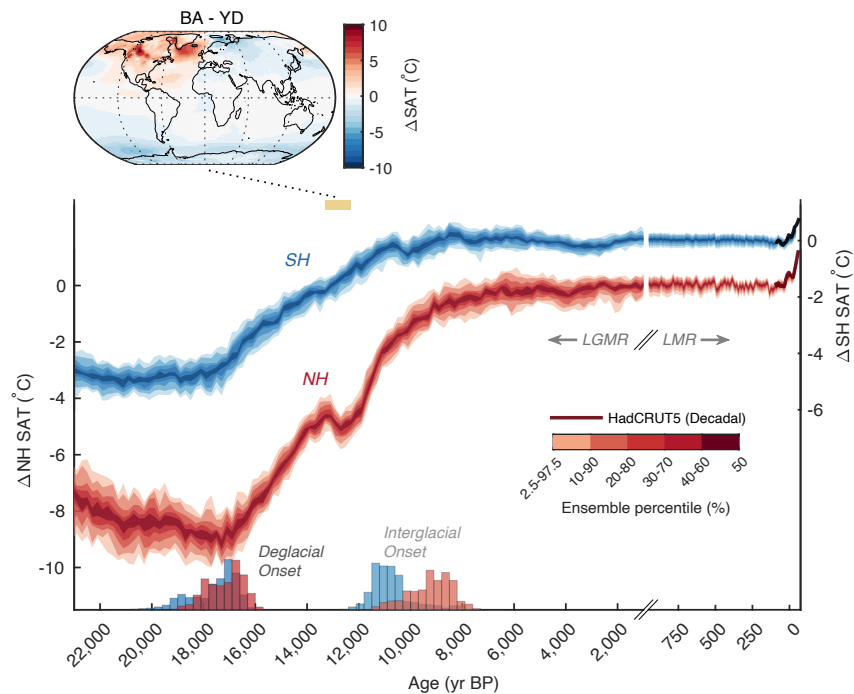
Extended Data Figure 4. Time-comparison of posterior LGMR with $\delta^{18}O_p$ with selected $\delta^{18}O_p$ ice core and speleothem records. Uncertainty ranges denote the $\pm 1\sigma$ level (dark) and 95% confidence range from the LGMR ensemble. Also shown for comparison are the full range (shaded grey) and median iCESM time slice prior values (50 year means) for each site. See also Extended Data Table 2.



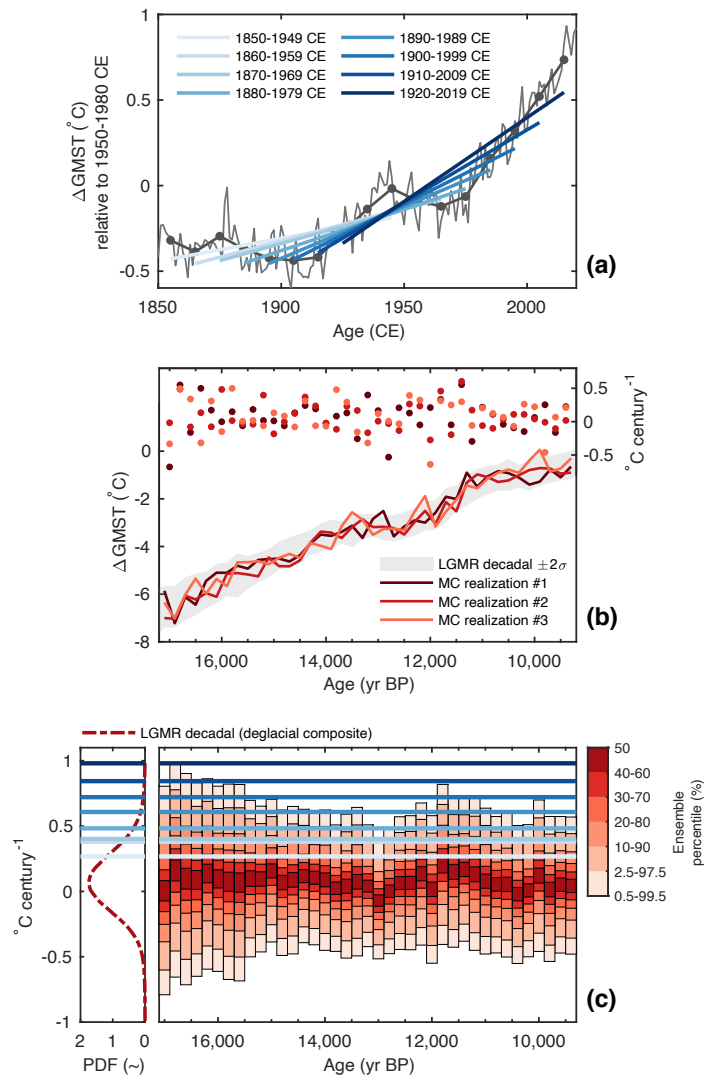
Extended Data Figure 5. Influences on global surface temperature evolution during the last 24 ka. Spatial LGM-to-present correlations between SAT and (a) combined greenhouse gas²⁶ and global albedo radiative forcing²⁸; (b) summer length at 65°S³¹; and (c) the $-1 \times \frac{^{231}\text{Pa}}{^{230}\text{Th}}$ AMOC proxy index from Bermuda Rise^{33–35} (shown such that SAT correlations are positive with AMOC strength).



Extended Data Figure 6. Proxy-specific GMST reconstructions. $\delta^{18}\text{O}_{calc}$ (a), $U_{37}^{K'}$ (b), and Mg/Ca (c). In (a-c), the shaded regions show the 95% confidence range across $n = 50$ ensemble members for the data assimilation derived GMST estimates, and $n = 10,000$ realizations for the proxy-only GMST estimates. All GMST curves from (a-c) are shown in (d) for side-by-side visualization.



Extended Data Figure 7. Hemispheric variability during the last 24 ka. Ensemble distribution ($n = 300$) of LGMR-estimated Northern Hemisphere (NH; red, adjusted by $+2^{\circ}\text{C}$ for improved visualization) and Southern Hemisphere (SH; grey) mean hemispheric temperatures during the last 24 ka. Shown at top is the surface temperature spatial difference for the Bølling-Allerød and Younger Dryas interval. Hemispheric last deglacial and interglacial onset timings are shown as histograms at bottom. The LGMR is plotted alongside reconstructed decadal hemispheric temperatures from the Last Millennium Reanalysis v2.1¹⁸ and HadCRUT5 observational product¹¹.



Extended Data Figure 8. Comparison between rates of warming in the LGMR and the recent historical record. (a) Observed centennial warming rates stepped decade-wise to present from HadCRUT5¹¹. (b) Example showing range of expected centennial-scale rates of deglacial warming (red scatter points) from three different Monte Carlo (MC)-based realizations of GMST change from the LGMR (red lines). Gray shading shows the decadal-adjusted LGMR $\pm 2\sigma$ range. (c) Comparison of observed (HadCRUT5) warming rates from (a) (horizontal blue lines) to the distribution of warming rates from the decadal-adjusted LGMR ensemble. Observed centennial warming rates after 1900 CE exceed the 99.9th percentile of LGMR deglacial warming.

Extended Data Table 1. Information on the iCESM simulations used for generating model priors. Greenhouse gas concentrations are in ppm for CO₂ and ppb for CH₄ and N₂O. Global mean seawater $\delta^{18}\text{O}$ ($\delta^{18}\text{O}_{sw}$) is in % relative to the Vienna Standard Mean Ocean Water (VSMOW). See *Methods* for details of the implementation of vegetation and freshwater forcing in related simulations.

Age (ka)	Model description	Number of priors	Greenhouse gas (CO ₂ /CH ₄ /N ₂ O)	Global $\delta^{18}\text{O}_{sw}$	Citation
0	iCESM1.2: PI	16	285 / 792 / 276	0.05	10
0	iCESM1.2: PI	10	285 / 792 / 276	0.05	56
0	iCESM1.3: PI	10	285 / 792 / 276	0.05	56
0	iCESM1.2 Last Millennium Member #2: 850-1850 CE	20	Transient	0.05	57
0	iCESM1.2 Last Millennium Member #3: 850-1850 CE	20	Transient	0.05	57
3	iCESM1.2: 3 ka	16	275 / 580 / 270	0.05	10
6	iCESM1.2: 6 ka w/ Sahara & 50–90°N greened	16	264 / 597 / 262	0.05	This study
6	iCESM1.2: 6 ka	8	264 / 597 / 262	0.05	This study
9	iCESM1.2: 9 ka w/ Sahara greened	16	260 / 659 / 255	0.34	This study
12	iCESM1.2: 12 ka	16	253 / 478 / 236	0.59	This study
12	iCESM1.2: 12 ka w/ freshwater over N. Atl.	4	253 / 478 / 236	0.59	This study
14	iCESM1.2: 14 ka	16	238 / 637 / 255	0.73	This study
16	iCESM1.2: 16 ka	16	224 / 452 / 199	0.90	This study
16	iCESM1.2: 16 ka w/ freshwater over N. Atl.	4	224 / 452 / 199	0.90	This study
18	iCESM1.2: 18 ka	16	190 / 370 / 245	1.02	10
21	iCESM1.2: 21 ka	16	190 / 375 / 200	1.05	10
21	iCESM1.3: 21 ka	18	190 / 375 / 200	1.05	56

Extended Data Table 2. Geographical and site identification information for ice core and speleothem $\delta^{18}\text{O}_p$ records used for LGMR external validation.

Proxy class	Site name	Lat. (°N)	Lon. (°E)	R²	CE	Citation
Ice core	Byrd	-80.02	-119.53	0.82	-0.71	72
Ice core	EDC	-75.10	123.35	0.89	0.49	73
Ice core	EDML	-75.00	0.07	0.86	0.78	73
Ice core	Fuji	-77.32	38.70	0.83	0.66	74
Ice core	Siple	-81.65	-149.00	0.88	0.64	75
Ice core	TALDICE	-72.82	159.18	0.89	0.76	76
Ice core	Taylor	-77.78	158.72	0.65	-0.65	77
Ice core	Vostok	-78.46	106.84	0.88	0.85	78
Ice core	WAIS	-79.47	-112.00	0.87	0.22	79
Ice core	Renland	71.27	-26.73	0.74	0.20	80
Ice core	GISP2	72.60	-38.50	0.65	0.05	81
Ice core	GRIP	72.58	-37.63	0.58	-0.21	82
Ice core	NGRIP	75.10	-42.33	0.71	0.55	83
Speleothem	Cold Air cave	-24.00	29.18	0.08	-14.58	84
Speleothem	Jaraguá cave	-21.08	-56.58	0.27	-1.63	85
Speleothem	Jeita cave	33.95	35.65	0.01	-15.69	86
Speleothem	Mawmluh cave	25.26	91.88	0.42	-4.47	87
Speleothem	Liang Luar cave	-8.53	120.43	0.06	-5.19	88
Speleothem	Bukit Assam cave	4.03	114.80	0.04	-5.23	89
Speleothem	Xiaobailong cave	24.20	103.36	0.20	-3.55	90
Speleothem	Sofular cave	41.42	31.93	0.04	-1.86	91
Speleothem	Botuverá	-27.22	-49.16	0.10	-7.88	92
Speleothem	Gunung-buda cave	4.03	114.80	0.02	-2.66	89
Speleothem	Nettlebed cave	-41.25	172.63	0.27	-4.11	93
Speleothem	Soreq cave	31.76	35.02	0.17	-5.45	94
Speleothem	El Condor cave	-5.93	-77.30	0.02	-0.42	95

Extended Data Table 3. External validation statistics associated with different choices of covariance localization and the 1σ "length-scale" range of the evolving prior sampling. ΔR^2 and $\Delta RMSEP$ values denote the change in observed vs. posterior assimilated $\Delta\delta^{18}O_p$ values relative to the prior iCESM estimated values; larger ΔR^2 and smaller $\Delta RMSEP$ thus denote greater improvement in the assimilated posterior relative to iCESM (see Extended Data Figure 2i-j for plotted LGMR values). For localization testing, listed ΔR^2 and $\Delta RMSEP$ values represent the median across all ($n = 6$) length-scale tests; for length-scale testing, listed ΔR^2 and $\Delta RMSEP$ values represent the median across all ($n = 8$) localization tests.

Localization (km) :	6,000	9,000	12,000	15,000	18,000	21,000	24,000	∞
ΔR^2	0.09	0.19	0.23	0.24	0.24	0.25	0.25	0.16
$\Delta RMSEP$ (‰)	-0.54	-0.59	-0.63	-0.63	-0.64	-0.72	-0.73	-0.34
Length scale (yr) :	2,000	3,000	4,000	5,000	6,000	∞		
ΔR^2	0.23	0.24	0.25	0.24	0.23	0.18		
$\Delta RMSEP$ (‰)	-0.63	-0.62	-0.64	-0.65	-0.69	-0.58		